2014

Multifunctional Skin-Like Electronics for Quantitative, Clinical Monitoring of Cutaneous Wound Healing

Yoshiaki Hattori
University of Illinois at Urbana-Champaign

Leo Falgout
University of Illinois at Urbana-Champaign

Woosik Lee
University of Illinois at Urbana-Champaign

See next page for additional authors

Copyright © 2014 WILEY-VCH Verlag GmbH & Co. KGaA, Weinheim. This is the peer reviewed version of the following article: Hattori, Y., Falgout, L., Lee, W., Jung, S.-Y., Poon, E., Lee, J. W., Na, I., Geisler, A., Sadhwani, D., Zhang, Y., Su, Y., Wang, X., Liu, Z., Xia, J., Cheng, H., Webb, R. C., Bonifas, A. P., Won, P., Jeong, J.-W., Jang, K.-I., Song, Y. M., Nardone, B., Nodzenski, M., Fan, J. A., Huang, Y., West, D. P., Paller, A. S., Alam, M., Yeo, W.-H. and Rogers, J. A. (2014), Multifunctional Skin-Like Electronics for Quantitative, Clinical Monitoring of Cutaneous Wound Healing. Advanced Healthcare Materials, 3: 1597–1607. doi: 10.1002/adhm.201400073, which has been published in final form at http://dx.doi.org/10.1002/adhm.201400073. This article may be used for non-commercial purposes in accordance with Wiley Terms and Conditions for self-archiving.

Authors

Yoshiaki Hattori, Leo Falgout, Woosik Lee, Sung-Young Jung, Emily Poon, Jung Woo Lee, Ilyoun Na, Amelia Geisler, Divya Sadhwani, Yihui Zhang, Yewang Su, Xiaoqi Wang, Zhuangjian Liu, Jing Xia, Huanyu Cheng, R. Chad Webb, Andrew P. Bonifas, Philip Won, Jae-Woong Jeong, Kyung-In Jang, Young Min Song, Beatrice Nardone, Michael Nodzenski, Jonathan A. Fan, Yonggang Huang, Dennis P. West, Amy S. Paller, Murad Alam, Woon-Hong Yeo, and John. A. Rogers

Title: Multifunctional Skin-like Electronics for Quantitative, Clinical Monitoring of Cutaneous Wound Healing

Woon-Hong Yeo

Prof. W. -H. Yeo
Department of Mechanical and Nuclear Engineering and Center for Rehabilitation Science and Engineering
Virginia Commonwealth University
Richmond, VA 23284, USA
E-mail: whyeo@vcu.edu

Keywords: wound monitoring, clinical study, skin-like, multifunctional, epidermal electronics

Non-invasive, biomedical devices have the potential to provide important, quantitative data for the assessment of skin diseases and wound healing. Traditional methods either rely on qualitative visual and tactile judgments of a professional and/or data obtained using instrumentation with forms that do not readily allow intimate integration with sensitive skin near a wound site. Here we report a skin-like electronics platform that can softly and reversibly laminate perilesionally at wounds to provide highly accurate, quantitative data of relevance to the management of surgical wound healing. Clinical studies on patients using thermal sensors and actuators in fractal layouts provide precise time-dependent mapping of temperature and thermal conductivity of the skin near the wounds. Analytical and simulation results establish the fundamentals of the sensing modalities, the mechanics of the system, and strategies for optimized design. The use of this type of 'epidermal' electronics system in a realistic, clinical setting with human subjects establishes a set of practical procedures in disinfection, reuse, and protocols for quantitative measurement. The results have the potential to address important unmet needs in chronic wound management.

1. Introduction

Monitoring of wound healing, a dynamic interactive biological process involving blood cells, extracellular matrix, and parenchymal cells, is of great interest in biomedical research and clinical practice. The most comprehensive means for assessment of wound healing is based on histological evaluation of tissue morphologic change,[1, 2] but this process is invasive and does not provide a means for continuous evaluation over time. Visual inspection by digital photography[1, 3, 4] overcomes these limitations, however interpretation is inherently subjective and the imaging often yields inconsistent information due to variations in lighting, focus and angle. Quantitative imaging methods via confocal laser scanning microscopy or spectroscopy can reveal microscopic level changes in the morphology of the epidermis and dermis.[4, 5] These methods, however, require patient immobilization during the testing. Also, the required sophisticated optical systems are high in cost and require trained personnel for evaluation. Recent work on simple, portable, point-of-care (POC) devices[1, 6] for optical sectioning and topical determination of wound healing phases suggest promise, although their use is ultimately limited by qualitative visual evaluation. In wound healing, calor is a primary indicator of inflammation and possible infection.[1, 7, 8] Hydration is another factor that affects wound healing.[7] Thus, monitoring of skin temperature and thermal conductivity (hydration), along with numerous other potential markers such as bacterial load, cytokine release, DNA, enzymes, hormones, pH, oxygen, and transepidermal water loss, [1] provides important clinical information.

Practical biomedical devices, capable of non-invasive, quantitative and multifunctional measurements of the healing process, are needed to complement optical and other techniques. In this communication, we introduce a skin-like electronics system capable of precise and real-time monitoring of cutaneous wound healing in a clinical setting. These devices represent a type of epidermal electronics system (EES),[8] which adopts the soft mechanical texture of the epidermis to allow conformal lamination and reversible bonding to the epidermis via van der Waals interactions alone.[9-11] The result is a natural, non-irritating and high quality interface to the skin that does not constrain natural motions or induce any discomfort.[10] EES can be designed in biocompatible, waterproof forms that are easily disinfected for clinical applications, enabling re-use. The sensors demonstrated here use microscale, metal traces in fractal layouts on soft, elastomeric membranes, capable of measurement and mapping of skin temperature with an accuracy comparable to that of a high-end infrared (IR) camera, with the additional capabilities of recording thermal conductivity and delivering precise levels of heating.

In wound healing monitoring, an EES records time-dynamic temperature and thermal conductivity of the skin tissue. Mapping of skin temperature is important because it presumably is capturing the ‘inflammation’ phase of the healing process, related to increased blood flow to the wound.[12, 13] Thermal conductivity correlates strongly to hydration state, which is another important aspect of wound care, and can serve as an early sign of the emergence of local edema.[14-16] From a practical standpoint, thermal conductivity can also serve as a sensitive indicator of quality of contact between the device and the wound, allowing the healthcare professional to assess proper mounting on the skin. Three dimensional mechanical and thermal simulations of this type of EES on human skin, through the finite element method (FEM) and the finite volume method (FVM), respectively, capture the underlying physics of this contact, as well as the mechanisms for physiological sensing mechanism. The results establish critical design criteria for clinical applications.

2. Results

2.1 Device design and mechanics modeling

Figure 1a presents a schematic view of the layouts of a multifunctional EES of the type used in the studies reported here. The device uses a multilayer construct that consists of metal traces with fractal geometries (Peano curve motif) in an interconnected collection of ultrathin filamentary serpentine (FS) interconnects and an open mesh configuration. Contact pads provide connection points to external data acquisition hardware. The fractal configuration offers superior elastic stretchability compared to conventional meandering structures[17] and, in the context reported here, enables precise thermal measurements in ways that are largely unaffected by mechanical strains associated with mounting onto the complex cutaneous wound shapes on the skin. Finite element modeling (FEM) analysis (*Supplementary Note 1 and Figure S1*) illustrates quantitatively the elastic properties of the fractal geometry chosen for present purposes, with a comparison to other fractal options, as well as conventional designs such as regular curves and serpentines. The sensors are integrated onto thin silicone membranes (dyed black to facilitate control measurements of temperature with an IR camera) by the techniques of transfer printing, and subsequently coated with an encapsulating layer of silicone. [18] The resulting EES offers effective elastic moduli (22.1 kPa, measured by DMA Q800, TA instruments, USA) significantly lower than the epidermis (100-150 kPa). Figure 1b – 1e shows the response upon 30 % uniaxial stretching (Figure 1b), multimodal folding (Figure 1c), biaxial stretching and twisting (Figure 1d), and 720° twisting (Figure 1e).

The device fabrication follows procedures described briefly in the Methods section, with details in *Supplementary Note 2 and Figure S2 and S3*. The process exploits conventional microfabrication techniques to form electronic structures on a silicon wafer coated with a sacrificial polymer, as a temporary carrier substrate. The conducting elements use 3 µm-thick copper (Cu) traces deposited by electron-beam evaporation. Layers of polyimide (PI; 1.2 µm in thickness, Sigma-Aldrich, USA) above and below place the Cu fractal (width: 35 µm) and FS traces (width: 50 µm) at the neutral mechanical plane (NMP) to minimize the bending strains. Water soluble tapes pick up the electronic patterns from the carrying wafer and transfers to a silicone membrane (500 µm in thickness, ~20 kPa in modulus; Ecoflex, Smooth-On, USA; Figure 1a). [10] A 5 µm thick layer of silicone spin cast on top of the device encapsulates the EES to provide a water-proof surface capable of sterilization for use in clinical studies with human patients. [18]

Figure 1f (top view) and 1g (tilted view) show microscale X-ray coherent tomography images (microXCT, Xradia, USA) of such a device. [19] The fractal construct accommodates levels of mechanical strain upon biaxial, radial stretching that exceed maximum values (~30 %) typically experienced in the skin. [8] Details of the microXCT imaging process appear in the *Supplementary Note 3*. FEM analysis (details in *Supplementary Figure S4*) and experimental studies with microXCT (Figure 1h) reveal that the fractal systems can be stretched elastically, with reversible mechanics, by ~15 % and ~30% with only 0.25 % and 0.85 % maximum principal strain in the Cu (elastic strain of Cu: 0.3 %; fracture strain of Cu: 5%),[20-22] respectively. The results (Figure 1h) suggest ability to ensure consistent, reproducible device function and operation at and beyond levels of deformation that can be tolerated by the skin (10 – 20 %).[9, 18]

2.2 Multifunctional characteristics

Figure 2 summarizes the hardware and capabilities of an integrated collection of components, consisting of data acquisition systems and an EES with an array of sensors and actuators, configured for multipoint mapping of temperature and thermal conductivity. The devices include an EES (wound compatible device), a current source (6221, Keithley Instruments, USA), a lock-in amplifier (SR830, Stanford Research Systems, USA), a multiplexer (FixYourBoard.com, U802, USA), and a laptop (Figure 2a). A thin, flexible ribbon cable (HST-9805-210, Elform, USA) connects the array of six sensors/actuators in the EES to a multiplexer that enables sequential operation for spatial recording of temperature and thermal conductivity. The measurement uses a four point-probe technique for determining voltage drop in the sensors[17] upon changes in temperature or mechanical strain (*Supplementary Figure S5*). Figure 2b lists representative operating parameters for the lock-in amplifier in thermal conductivity and temperature measurements. Custom software presents a user-friendly interface that automatically calculates relevant parameters from voltages recorded through a GPIB cable interface (NI GPIB-USB-HS, National Instruments Corp., USA) to the computer. Changes in electrical resistance of the fractal constructs allow determination of changes in temperature, through a calibration curve (Figure 2c) established using data from an IR camera (precision <50 mK, A655SC, FLIR, USA) and a precisely controlled hot plate (details in *Supplementary Note 4*). The resistance is calculated by measured voltage drop in the sensors. The measured precision of an EES is ~50 mK, determined by limitations in the analogue-to-digital converter. Absolute accuracy in clinical testing is ~200 mK, determined by the use of the constant current source.

Evaluation of thermal conductivity uses an alternating current (AC) method adapted from techniques previously used in other contexts, known as the 3 omega (3ω) method. [23] Here, an AC current applied to the fractal structures induces both heating and changes in resistance that, in turn, influence the heating levels. This nonlinear coupling leads to a voltage output at the third harmonic of the AC drive. The magnitude of this signal is influenced by the thermal conductivity of the contacting material, i.e. the human skin. Details of the measurement schemes and calibration procedures in this case appear in *Supplementary Note 5*. The frequency dependence of the 3ω voltage signals for operation in air and the associated amplitude of the temperature oscillations appear in *Supplementary Figure S7 and S8*, respectively. 3ω voltages measured at two different AC frequencies can be used with a simple analytical expression to determine the thermal conductivity: [23]

$$\lambda = \frac{R_0 I_{rms}^3 \ln(f_H / f_L)}{4l\pi(V_{3\omega L} - V_{3\omega H})} \frac{dR}{dT} \tag{1}$$

where R_0 is the nominal resistance of the sensor, I_{rms} is the applied root-mean-square (RMS) current at 1ω, f_H is a selected higher frequency, f_L is a lower frequency, l is the length of the sensor, and $V_{3\omega}$ is the measured RMS voltage at 3ω (L and H denote lower and higher, respectively), and dR/dT is resistance change as a function of temperature. Calibration with known values of thermal conductivity is required to account for various aspects of the device structure and non-linearity in the response. Chosen two frequencies in the measurement offer the best compromise of skin characterization and reduced time for clinical measurement on patients.

Figure 2d presents the calibrated relationship between the thermal conductivity measured using an EES for six examples where the conductivity is known (air, concentrations of 0, 25, 50, 75, and 100 % ethanol in water). [24] The measurements involve probing to effective depths that depend on various details, including the frequency, as illustrated in results of Figure 2e obtained by numerical analysis for the case of a simplified model of human skin. Here, a quasi-steady-state form of the heat conduction equation can be solved at the operating frequency by the finite volume method (FVM) with the 2D approximations[25] (details in *Supplementary Note 6 and Table S1*). The amplitude of oscillation temperature on the fractal sensor (Figure 2e) decreases sharply from the EES and skin contact, and later converges in the dermis layer. The characteristic distribution of these curves follows expected patterns as reported earlier. [26] For frequencies used in our clinical studies (i.e. $V_{3\omega L}$ = 1 Hz and $V_{3\omega H}$ = 3 Hz), the measured thermal conductivity is influenced by properties of both the epidermis and dermis.

We note that the heating functionality needed for assessment of thermal conductivity might be advantageous separately in a therapeutic mode. The steady-state temperature distribution associated with Joule heating is important in this context. Modeling of the well-known Pennes bioheat transfer equation, with FVM and 2D approximations (*Supplementary Note 7*), yields results shown in Figure 2g. Figure 2h presents calculated temperature distributions for various input currents, where increased temperature can be observed down to the dermis layer. Applied currents (35, 50, and 65 mA) yield peak temperatures of 38, 42, and 46 ℃, respectively. These temperatures can be measured and controlled accurately by using the heaters simultaneously as temperature sensors. This study indicates, therefore, some potential of an EES for therapeutic use since local heating is known to promote healing of chronic wounds[27, 28] and has been used in hyperthermia treatment of some skin cancers.[27, 29-31]

2.3 Device characterization

The mechanical, thermal and measurement properties are critical to the operation of these types of devices. For example, mechanical deformations can induce strains in the sensors, with the potential to change their resistances in ways that might confound temperature and thermal conductivity measurements. This effect can have practical importance, simply because uniaxial stretching and multimodal bending can occur in the process of applying and removing the device from skin. These mechanical deformations may also cause slight, permanent changes in the resistance of the sensors by plastic deformation. Fractal choices in layout, guided by FEM analysis of the mechanics, can minimize such effects. [17] **Figure 3a** shows the contribution of cyclic uniaxial loading to a maximum elongation of 15 %. The device is first stretched to 15 % and then released back to 0 % (details in *Supplementary Note 8*). The measurements reveal elastic elongation and release response without hysteresis in the stress-strain curve (Figure 3a). The resistance change of 0.025 % at 15 % elongation changes the apparent temperature reading by only 0.05 ℃. Figure 3b shows that temperature changes due to bending are negligible (temperature shift: < 0.01 ℃) in the bending radius between 15 and 45 mm. Results indicated relatively small effects of deformation on thermal measurement; further reductions are possible with refined device designs.

Direct and simultaneous comparison of temperature recordings using an EES and IR camera supports the accuracy and reproducibility of measurements of temperature, as outlined in *Supplementary Note 9*. Figure 3c presents an IR thermogram of a forearm with an EES laminated on the skin, revealing increased temperature in locations of arteries. Figure 3d compares temperature distributions on the skin measured from using the EES with that from an IR camera. Due to thermal convection on the air-exposed surface of the device, the skin temperature from an EES is slightly higher than (0.6±0.4 ℃) that from the IR thermogram. The shifted IR thermogram temperature matches well with EES data. The thermal conductivity must be assessed independently, as this quantity cannot be determined with the IR camera. Figure 3e presents a measurement on the forearm with a wet piece of paper under sensor #3. The locally increased thermal conductivity results in an expected increased thermal conductivity reading from this sensor. Other sensors yield values that are typical epidermis thermal conductivity values (0.1 - 0.3 W/mK) (Figure 3f).

For practical application in the clinic, these measurement capabilities must not be altered by standard procedures for disinfection of devices that are placed on the skin, such as rubbing the application area with isopropyl alcohol antiseptic. [32-34] Per protocol, each EES was prepared immediately prior to use (details in *Supplementary Note 10 and Figure S19*). Device functions were verified with multiple cleaning steps for repetitive use demonstration, by recording thermal conductivity values at three different conditions. The graph in Figure 3g presents measurement results after cleaning procedures with air exposure, 50 % ethanol/water mixture, and acrylic board (OPTIX, Plaskolite, USA) over multiple cycles of cleaning. Values in all cases are consistent with the known thermal conductivity values, indicated by the straight lines. Related evaluations on the skin can be accomplished by examining repeatability in measurements performed at a single anatomic site. Figure 3h shows thermal conductivity values from 20 measurements. Results show good consistency, with a precision of ~4 %. This result is important because it suggests that the soft construction of the EES allows conformal contact with the surface of the skin, consistent with previous observations in other contexts. [16] The interfacial contact adhesion between the EES and the skin was measured as ~0.5 N/m from the mechanical peel tests using a force gauge (Mark-10, USA).[10]

2.4 Use of EES on human subjects in a clinical setting

Adhesion and skin irritation of the EES vs. conventional medical skin tape (3M, USA; major ingredient, acrylate polymer)[10] was determined after mounting on the forearm (**Figure 4a** – 4g). Observation of the skin by a digital contact microscope (AM7013MT Dino-Lite, AnMo Electronics, USA) after mounting was used to assess skin irritation (erythema and scaling) qualitatively. Despite more than 30 episodes of mounting and removal on the same anatomic skin site, EES did not cause any clinical evidence of irritation (Figure 4a and 4b). In contrast, acrylate-based medical tape caused slight erythema upon removal from the skin (Figure 4c-1), likely due to partial exfoliation of stratum corneum by the adhesive (Figure 4c-2). The silicone surface of the EES has hydrophobic methyl groups, unlike the hydrophilic surface of the acrylate tape, which presents hydroxyl groups (Figure 4d and 4e). The general, non-covalent interfaces of the EES offer sufficient adhesion for conformal contact (Figure 3h), similar to the adhesion of dry skin adhesives.[35-38] To further assess the potential impact of EES on keratinocyte (skin cell) viability, normal human keratinocytes were seeded onto the EES and viability was tested with a live/dead staining assay kit. Fluorescence microscopic images show that most cells cultured on the EES remain viable (stained as 'red')[39-41] (Figure 4f).

Three subjects undergoing incisional cutaneous wounding for skin lesions were enrolled (Figure 4g and 4h). Two devices were used: one in proximity to the surgical wound site and the other at the comparable area on the contralateral side as a control for evaluating time dynamic natural variations in body temperature. Optimization of the system construction and recording parameters enabled rapid, multi-point evaluation of temperature and thermal conductivity, as well as comparison of the former results simultaneously obtained with an IR camera, everything within only 10 minutes (Figure 4i). **Figure 5a** presents images at day 1, 3, 15, and 30 with the EES in intimate contact perilesionally to the cutaneous wound and can be compared with IR thermography at a single time point for comparison (Figure 5b). Measurements from the contralateral site are in *Supplementary Figure S20*. The EES for temperature and thermal conductivity recording uses six sensing components with 45 mm long spatial coverage. Figure 5c presents variations in temperature recorded by the six sensors, as shown by arrows (inset) from day 1 to day 30. The normalized data (Figure 5c, right) demonstrates relative temperature difference adjacent to the wound site compared with normal skin. The sudden temperature rise on day 3, as indicated in the graph, captures the inflammation phase, which is thought to be due to increased blood flow and enzymatic reactions. [1, 12, 13, 42] The control experiment (Figure 5d) on the contralateral site measures the baseline temperature without wounding. The measurement of localized, tissue thermal conductivity with the same device enables the assessment of conformal contact and skin hydration (Figure 5e). [16] On day 3 when the wound is considered to be in the inflammation phase, the corresponding thermal conductivity is slightly lower than at other time frames. To our knowledge, no previous studies have reported such subtle hydration variation, especially on hypersensitive wound tissue, during the wound healing process. Other works regarding hydration monitoring have typically focused only on the effect of balancing the hydration level in wound healing, [1] dressing materials, [43] or as *in vitro* only testing with a simulated wound bed. [7]

One subject (Subject 3) had a long surgical incision with suturing (**Figure 6**), protected by a dressing for the first two post-surgical weeks (Figure 6a). IR thermography captured temperature change for comparison with data obtained with the EES (Figure 6b). Another subject (Subject 1) had a granulating wound which showed elevated calor on day 3, but also temperature elevation on day 15 (Figure 6c), perhaps reflecting prolonged, more intense inflammation. [1, 12, 44] Temperature variation near the wound site was clearly and reproducibly distinguishable from the minimal variance of the contralateral, control body temperature (Figure 6d). In the sutured wound, the extended inflammation phase demonstrated stable thermal conductivity during a prolonged period and differed from the temperature pattern of the granulating wound (Figure 6e). Temperature and thermal conductivity change on the contralateral site are shown in *Supplementary Figure S21*. Subject 2, also with a granulating wound, showed a similar trend in measurements to Subject 1 (Table 1 and *Supplementary Figure S22*).

3. Discussion

Stretchable, conformal, multifunctional system design and layouts, in unusual forms, enable quantitative physiological measurements in patients, an innovation in cutaneous wound management. The stretchable electronic device offers material and mechanical properties that are well-matched to human skin, allowing new levels of integration of biotic and abiotic systems that was previously precluded by hard, flat or merely flexible devices. Biocompatible, ultra-soft silicone completely encloses the electronics system (effective moduli: ~22 kPa, thickness: ~500 μm) to provide enhanced gentle wearability on hypersensitive wound tissue, simple disinfection, and re-use capabilities that are favorably required in the clinical setting. Multimodal functions, design criteria, and spatial mapping of physiological assessment on the skin by an EES, well-understood and supported by three dimensional FEM and FVM analysis in mechanics and thermodynamics, opens a new route for continuous, quantitative, long-term monitoring in clinical wound management.

Possible improvement includes a new device configuration in an ultra-thin, more compliant but robust set that can be directly laminated over a wound tissue for wound management without interference of natural skin interface. More functions to monitor electromyogram, pH level, mechanical strain change, and transepidermal water loss can be added into the multifunctional electronics. Another set of devices with purely based on thermochromic polymers without electric circuits, along with a simple digital imaging, would enable a cheap, portable, but quantitative monitoring of skin temperature without the use of sophisticated electronic devices and signal filtering/processing. Furthermore, incorporation with a wireless powering and transmission system that has integrated circuits in stretchable forms would deliver the ultimate concept of home-setting assessment of wound management, as in a smart healthcare system.

4. Conclusion

In conclusion, this communication has introduced the use of a multifunctional, conformal EES in cutaneous wound management for patient applicability. Sets of micro-metal resistors demonstrated the multimodal measurement of high precision skin temperature, thermal conductivity in disinfected, re-use configuration and also showed the actuation function as micro-heaters. This class of technology is expanded further, with the support of three dimensional finite element methods, to address unresolvable needs that include biocompatible, noninvasive, continuous monitoring of skin physiology in chronic wound management.

5. Experimental Section

Fabrication of an EES: The device processing used conventional microfabrication techniques (details in *Supplementary Note 2 and Figure S2 and S3*). A carrier substrate was prepared by spin coating thin layers of polydimethylsiloxane (PDMS; 10 μm in thickness, Dow Corning, USA) and polyimide (PI; 1.2 μm in thickness, Sigma-Aldrich, USA) on a 3 inch silicon wafer. Electron beam evaporation formed 3 μm-thick layers of Cu on the substrate. Photolithography and etching defined the fractal and FS traces. A water soluble tape (3M, USA) retrieved the completed patterns from the carrier wafer, for subsequent transfer and covalent bonding onto a black silicone membrane (Ecoflex, Smooth-On, USA). To provide electrical isolation for clinical use, a 5 μm-thick layer of silicone was coated on top of patterns. For data acquisition, a flexible, anisotropic ribbon cable made electrical contact to the connection pads.

Biaxial stretching and imaging: Biaxial mechanical stretching of a fractal sensing component of an EES involved mounting onto a home-made plate with circular opening above an air chamber. Connecting the chamber to an external pump allowed controlled adjustment of biaxial strain induced by inflation. Three dimensional, micro X-ray tomography (Xradia, USA) was used to image microscale behaviors of the fractal traces (details in *Supplementary Note 3*).

Clinical study on patients: All experiments on patients were conducted under a protocol (number: STU69718) approved by the Institutional Review Board, Northwestern University, Chicago, IL, USA. Prior to study entry, subjects signed written informed consents per adherence to Helsinki Guidelines. Research was carried out in a clinical exam room at the central Northwestern Medical Group Dermatology Clinic (676 North St. Clair Street, Suite 1600, Northwestern University, Feinberg School of Medicine, Chicago, IL, USA).

Supporting Information

Supporting Information is available from the Wiley Online Library or from the author.

Acknowledgements

W.-H.Y. acknowledges the support of startup fund from the Virginia Commonwealth University.

References

[1] T. R. Dargaville, B. L. Farrugia, J. A. Broadbent, S. Pace, Z. Upton, N. H. Voelcker, *Biosens. Bioelectron.* **2013**, 41, 30.

[2] J. Panuncialman, S. Hammerman, P. Carson, V. Falanga, *J. Invest. Dermatol.* **2009**, 129, S47.

[3] C. T. Hess, R. S. Kirsner, *Advan. Skin Wound Care* **2003**, 16, 246.

[4] S. Lange-Asschenfeldt, A. Bob, D. Terhorst, M. Ulrich, J. Fluhr, G. Mendez, H. J. Roewert-Huber, E. Stockfleth, B. Lange-Asschenfeldt, *J. Biomed. Opt.* **2012**, 17, 076016.

[5] N. J. Crane, E. A. Elster, *J. Biomed. Opt.* **2012**, 17, 010902.

[6] T. Serena, Protease Activity Levels Associated with Healing Status of Chronic Wounds, http://www.systagenix.com/cms/uploads/NG42-11_Serena_et_al_Protease_Activity_Levels_Associated_with_Healing_Status_of_Chronic_Wounds_Wounds_UK_2011_004.pdf , **2011**.

[7] S. Guo, L. A. DiPietro, *J. Dent. Res.* **2010**, 89, 219.

[8] G. Matzeu, M. Losacco, E. Parducci, A. Pucci, V. Dini, M. Romanelli, F. Di Francesco, *Ieee Ind. Elec. (IECOn 2011)* **2011,** 3533.

[9] D. McColl, B. Cartlidge, P. Connolly, *Int. J. Surg.* **2007**, 5, 316.

[10] D. H. Kim, N. S. Lu, R. Ma, Y. S. Kim, R. H. Kim, S. D. Wang, J. Wu, S. M. Won, H. Tao, A. Islam, K. J. Yu, T. I. Kim, R. Chowdhury, M. Ying, L. Z. Xu, M. Li, H. J. Chung, H. Keum, M. McCormick, P. Liu, Y. W. Zhang, F. G. Omenetto, Y. G. Huang, T. Coleman, J. A. Rogers, *Science* **2011**, 333, 838.

[11] J. W. Jeong, W. H. Yeo, A. Akhtar, J. J. S. Norton, Y. J. Kwack, S. Li, S. Y. Jung, Y. W. Su, W. Lee, J. Xia, H. Y. Cheng, Y. G. Huang, W. S. Choi, T. Bretl, J. A. Rogers, *Adv. Mater.* **2013**, 25, 6839.

[12] W. H. Yeo, Y. S. Kim, J. Lee, A. Ameen, L. K. Shi, M. Li, S. D. Wang, R. Ma, S. H. Jin, Z. Kang, Y. G. Huang, J. A. Rogers, *Adv. Mater.* **2013**, 25, 2773.

[13] W. H. Yeo, R. C. Webb, W. Lee, S. Jung, J. A. Rogers, *Proc. Spie* **2013**, 8725.

[14] T. Helfman, L. Ovington, V. Falanga, *Clin. Dermatol.* **1994**, 12, 121.

[15] A. J. Singer, R. A. F. Clark, *New Engl. J. Med.* **1999**, 341, 738.

[16] X. Huang, H. Y. Cheng, K. L. Chen, Y. L. Zhang, Y. H. Zhang, Y. H. Liu, C. Q. Zhu, S. C. Ouyang, G. W. Kong, C. J. Yu, Y. G. Huang, J. A. Rogers, *Ieee T. Bio-Med. Eng.* **2013**, 60, 2848.

[17] X. Huang, W. H. Yeo, Y. H. Liu, J. A. Rogers, *Biointerphases* **2012**, 7, 52.

[18] R. C. Webb, A. P. Bonifas, A. Behnaz, Y. H. Zhang, K. J. Yu, H. Y. Cheng, M. X. Shi, Z. G. Bian, Z. J. Liu, Y. S. Kim, W. H. Yeo, J. S. Park, J. Z. Song, Y. H. Li, Y. G. Huang, A. M. Gorbach, J. A. Rogers, *Nat. Mater.* **2013**, 12, 1078.

[19] J. A. Fan, W.-H. Yeo, Y. Su, Y. Hattori, W. Lee, S. Jung, Y. Zhang, Z. Liu, H. Cheng, L. Falgout, M. Bajema, T. Coleman, D. Gregoire, R. Larson, Y. Huang, J. A. Rogers, Fractal Design Concepts for Stretchable Electronics. *Nat. Commun.*, DOI: 10.1038/ncomms4266, **2013**.

[20] J. W. Jeong, M. K. Kim, H. Cheng, W. H. Yeo, X. Huang, Y. Liu, Y. Zhang, Y. Huang, J. A. Rogers, *Adv. Healthc. Mater.* DOI: 10.1002/adhm.201300334, **2013**.

[21] Y. M. Song, Y. Z. Xie, V. Malyarchuk, J. L. Xiao, I. Jung, K. J. Choi, Z. J. Liu, H. Park, C. F. Lu, R. H. Kim, R. Li, K. B. Crozier, Y. G. Huang, J. A. Rogers, *Nature* **2013**, 497, 95.

[22] J. R. Davis, Asm Specialty Handbook: Copper and Copper Alloys, *ASM International*, **2001**.

[23] W. F. Riley, Sturges, L.D., and Morris, D.H., Mechanics of Materials, *John Wiley & Sons*, New York, **1999**.

[24] Y. H. Zhang, S. Xu, H. R. Fu, J. Lee, J. Su, K. C. Hwang, J. A. Rogers, Y. G. Huang, *Soft Matter* **2013**, 9, 8062.

[25] D. G. Cahill, *Rev. Sci. Instrum.* **1990**, 61, 802.

[26] M. J. Assael, E. Charitidou, W. A. Wakeham, *Int. J. Thermophys.* **1989**, 10, 793.

[27] S. R. Choi, D. Kim, *Rev. Sci. Instrum.* **2008**, 79, 064901.

[28] R. Q. Gram, A. She, R. S. Craxton, D. R. Harding, *J. Appl. Phys.* **2012**, 112, 033504.

[29] D. Haemmerich, P. F. Laeseke, *Int. J. Hyperthermia* **2005**, 21, 755.

[30] D. H. Kim, S. D. Wang, H. Keum, R. Ghaffari, Y. S. Kim, H. Tao, B. Panilaitis, M. Li, Z. Kang, F. Omenetto, Y. G. Huang, J. A. Rogers, *Small* **2012**, 8, 3263.

[31] C. J. Gannon, P. Cherukuri, B. I. Yakobson, L. Cognet, J. S. Kanzius, C. Kittrell, R. B. Weisman, M. Pasquali, H. K. Schmidt, R. E. Smalley, S. A. Curley, *Cancer-Am. Cancer Soc.* **2007**, 110, 2654.

[32] T. Juang, D. Neuman, J. Schlorff, P. R. Stauffer, ieee, in *Proceedings of the 26th Annual International Conference of the Ieee Engineering in Medicine and Biology Society, Vols 1-7*, Vol. 26, Ieee, New York, **2004**, 3467.

[33] Y. S. Koo, A. E. Fathy, R. Kazemi, J. Phillips, Ieee, in *2012 Ieee Antennas and Propagation Society International Symposium*, Ieee, New York, **2012**.

[34] Infection Control Manual, https://practicegreenhealth.org/pubs/sharing/SHC_InfectionControlPolicy_7%2010CleaningofEquipment.pdf (Stanford Hospital and Clinics), **2010**.

[35] G. McDonnell, A. D. Russell, *Clin. Microbiol. Rev.* **1999**, 12, 147.

[36] W. A. Rutala, D. J. Weber, *Centers for Disease Control and Prevention*, **2008**.

[37] J. M. Karp, R. Langer, *Nature* **2011**, 477, 42.

[38] M. K. Kwak, H. E. Jeong, K. Y. Suh, *Adv. Mater.* **2011**, 23, 3949.

[39] M. K. Kwak, C. Pang, H. E. Jeong, H. N. Kim, H. Yoon, H. S. Jung, K. Y. Suh, *Adv. Funct. Mater.* **2011**, 21, 3606.

[40] B. Laulicht, R. Langer, J. M. Karp, *P. Natl. Acad. Sci. USA* **2012**, 109, 18803.

[41] Y. J. Choi, S. Chae, J. H. Kim, K. F. Barald, J. Y. Park, S. H. Lee, *Sci. Rep.* **2013**, 3, 1921.

[42] H. C. Jung, J. H. Moon, D. H. Baek, J. H. Lee, Y. Y. Choi, J. S. Hong, S. H. Lee, *Ieee T. Bio-Med. Eng.* **2012**, 59, 1472.

[43] S. M. Lee, J. H. Kim, H. J. Byeon, Y. Y. Choi, K. S. Park, S. H. Lee, *J. Neural Eng.* **2013**, 10, 036006.

[44] C. P. Pan, Y. H. Shi, K. Amin, C. S. Greenberg, Z. Haroon, G. W. Faris, *Biomed. Opt. Express* **2010**, 1, 285.

[45] D. Queen, H. Orsted, H. Sanada, G. Sussman, *Int. Wound J.* **2004**, 1, 59.

Figure 1. Device design and mechanics modeling. (a) Schematic illustration of an EES. (b) Image of an device under uniaxial stretching , multimodal folding (c) and biaxial stretching and twisting (d) and 720° twisting (e). (f) Top view and tilted view (g) microXCT images of the device in (d). (h) FEM analysis and experimental study of a fractal construct under uniaxial stretching; FEM (top) and experiment (bottom). The inset in the middle illustrates the neutral mechanical plane (NMP) of the metal with polyimide (PI) encapsulation.

Figure 2. Multifunctional characteristics. (a) Data acquisition system. (b) Parameters of the lock-in amplifier for measurement of temperature and thermal conductivity. (c) Electrical resistance of six sensors in an EES, as a function of surface temperature. (d) Measurement of thermal conductivity by an EES. (e) Simulation of the oscillating temperature distribution induced in the skin by the EES. (f) IR thermography during Joule heating (35 mA) using one of the sensors in the EES as a micro-heater. (g) Simulation of the rise in temperature on the surface of the device upon Joule heating (35 mA). (h) Simulation of the rise in temperature on the skin tissue on the device surface upon Joule heating.

Figure 3. Device characterization. (a) Effect of mechanical stretching on the measured temperature. (b) Effect of bending on the measured temperature. (c) IR thermogram of the forearm with an EES mounted. (d) Temperature distribution on the skin measured by the IR camera and the EES along blue dotted line shown in (c). The horizontal axis shows the distance from the top of the heater. (e) EES mounted on the forearm with a wet paper towel that covers sensor #3. (f) Distribution of measured thermal conductivity of the skin. The value from sensor #3 shows a clear, expected difference from the other sensors. (g) Thermal conductivity of air, 50% ethanol and acrylic sheet measured after multiple cycles of cleaning. The straight lines in the graph show the actual values. (h) Thermal conductivity measured on the forearm with 20 measurements in one individual.

Figure 4. Use of an EES on human subjects in a clinical setting. (a) EES laminated on the skin (forearm) after sterilization. (b) Microscope images of the skin with thirty attempts of mounting and removal of an EES. (c) Microscope image of the skin after the medical tape removal (1) and image of the tape surface (2). (d) Illustration of the materials interface between the EES and skin (e) Illustration between the medical tape and skin. (f) Fluorescence images of viability of skin cells grown on an EES (left) and the control on the regular cell culture materials (right). Most of cells on the EES remain viable ('red' cells). (g) Clinical setting for wound monitoring in a typical exam room. (h) EES laminated on wound and contralateral (control) sites. (i) Assessment sequence and estimated time.

Figure 5. Quantitative monitoring of a granulating wound with an EES. (a) Representative photos of the wound with an EES from day 1 to day 30. (b) Corresponding IR images of the temperature distribution associated with (a). (c) Temperature distribution recorded with an EES (inset) from wound skin to normal skin during one month. The six sensors span a distance of 45 mm in lateral direction. (d) Temperature distribution on a contralateral side. (e) Thermal conductivity (T.C.) distribution recorded with three sensors in an EES (inset). (f) Thermal conductivity (T.C.) on a contralateral side as a control.

Figure 6. Quantitative management of sutured wound with an EES. (a) Representative photos of the wound with an EES from day 1 to day 30. (b) Corresponding IR images of the temperature distribution associated with (a). (c) Temperature distribution recorded with an EES (inset) from wound skin to normal skin during one month. The six sensors span a distance of 45 mm in lateral direction. (d) Temperature distribution on a contralateral side. (e) Thermal conductivity (T.C.) distribution recorded with three sensors in an EES (inset). (f) Thermal conductivity (T.C.) on a contralateral side as a control.

Table 1. Summary of clinical study with 3 subjects.

Figure 1

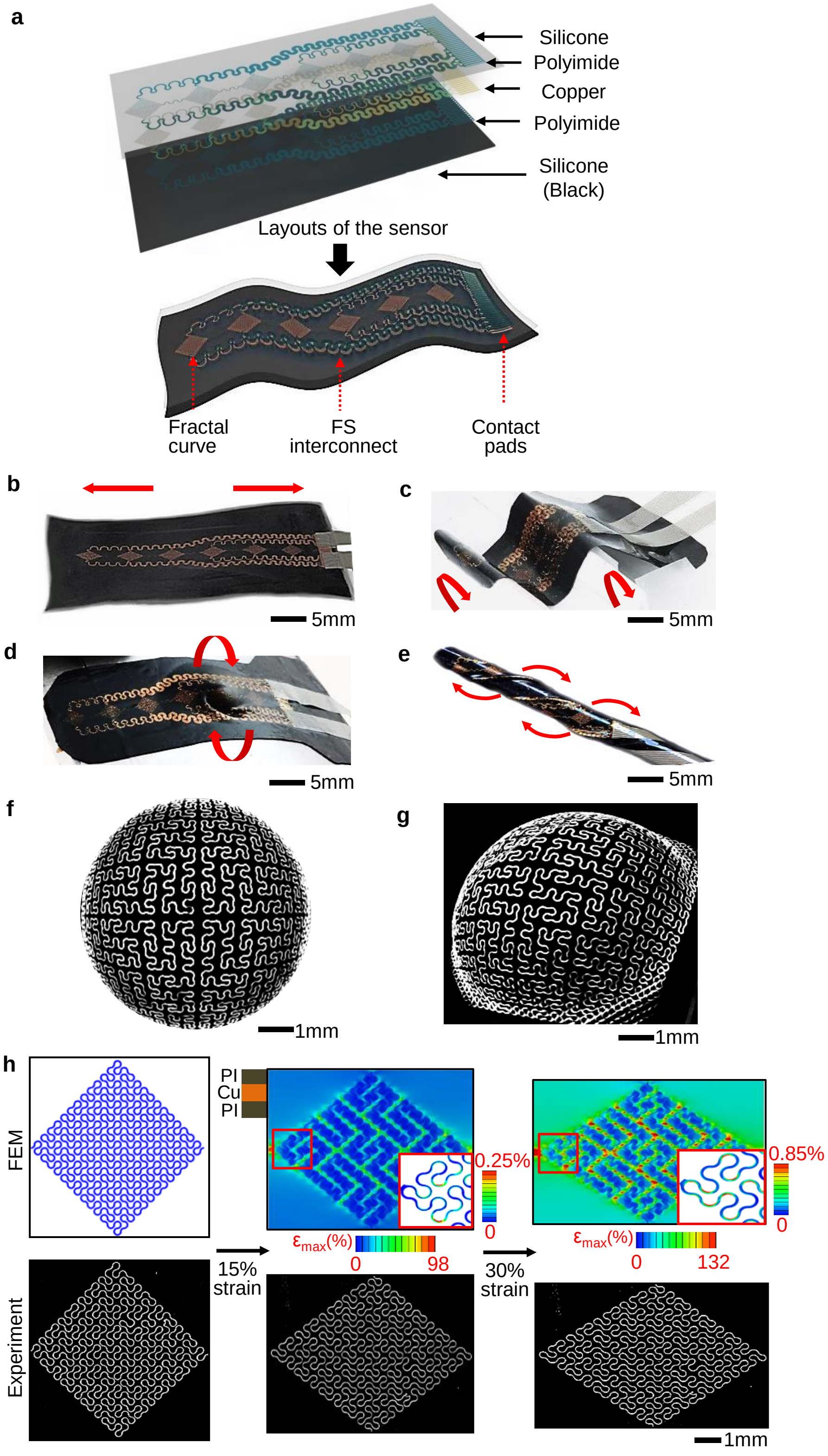
a
Silicone
Polyimide
Copper
Polyimide
Silicone (Black)
Layouts of the sensor
Fractal curve
FS interconnect
Contact pads
b
5mm
c
5mm
d
5mm
e
5mm
f
1mm
g
1mm
h
FEM
Experiment
PI
Cu
PI
15% strain
30% strain
0.25%
0
0.85%
0
εmax(%)
0
98
εmax(%)
0
132
1mm

Figure 2

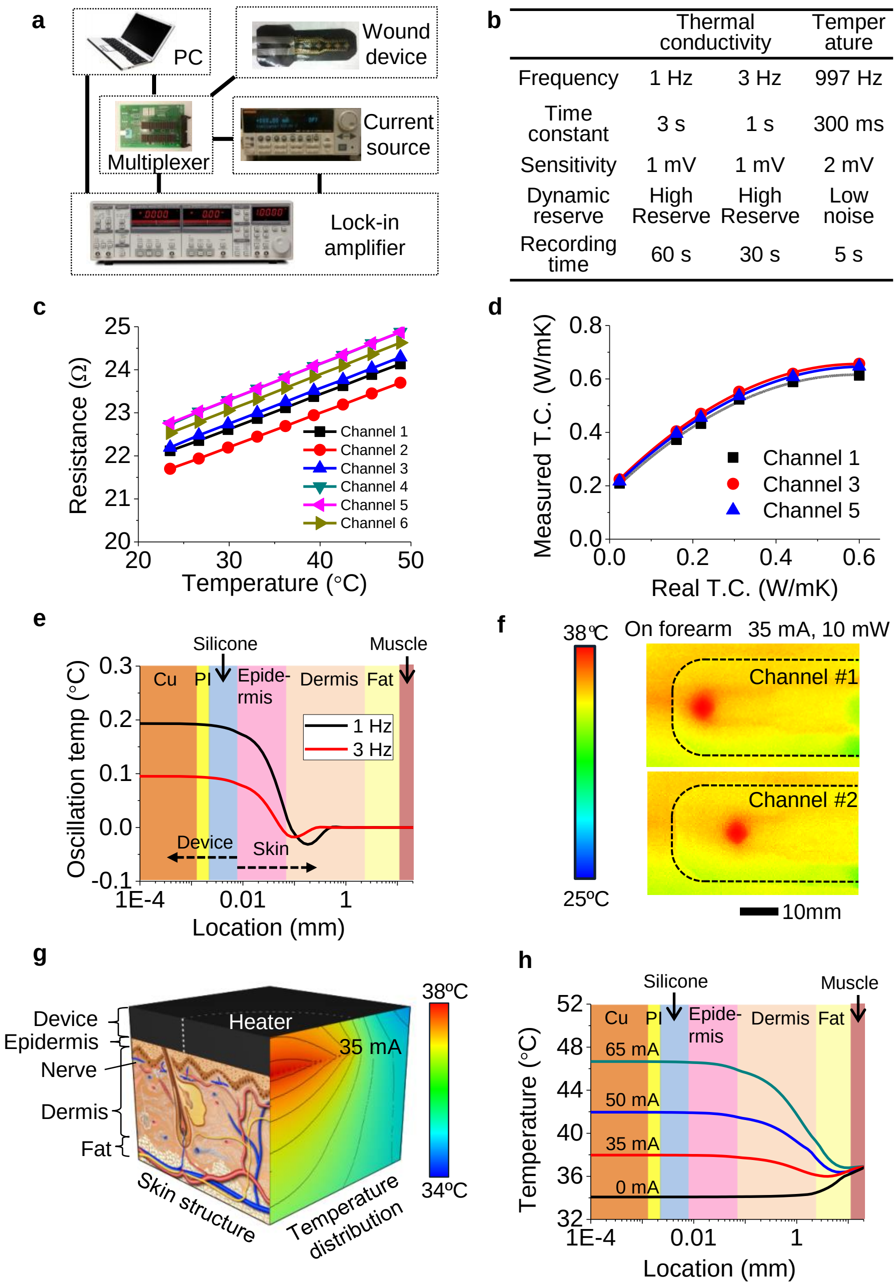

	Thermal conductivity		Temperature
Frequency	1 Hz	3 Hz	997 Hz
Time constant	3 s	1 s	300 ms
Sensitivity	1 mV	1 mV	2 mV
Dynamic reserve	High Reserve	High Reserve	Low noise
Recording time	60 s	30 s	5 s

Figure 3

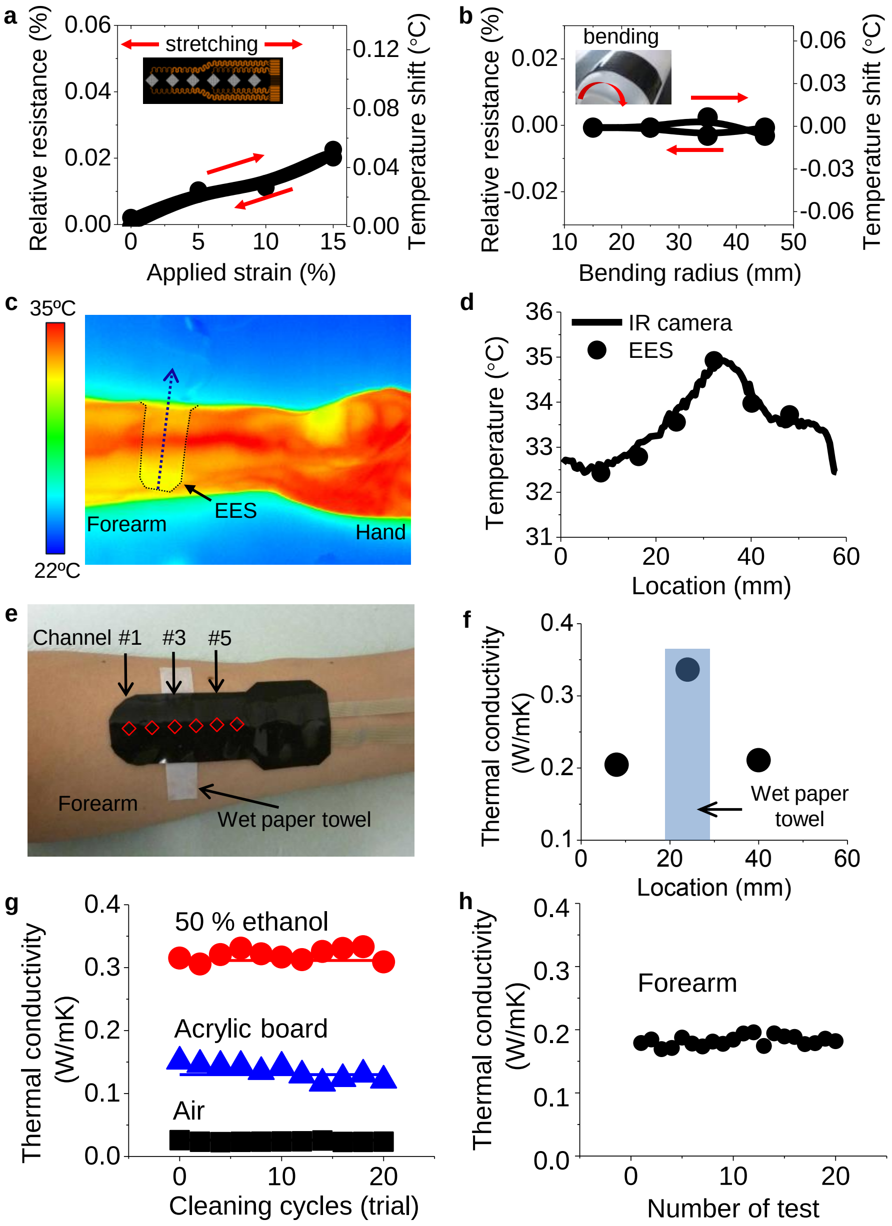
a
Relative resistance (%)
0.06
0.04
0.02
0.00
stretching
0
5
10
15
Applied strain (%)
0.12
0.08
0.04
0.00
Temperature shift (°C)
b
Relative resistance (%)
0.02
0.00
-0.02
bending
10
20
30
40
50
Bending radius (mm)
0.06
0.03
0.00
-0.03
-0.06
Temperature shift (°C)
c
35ºC
22ºC
Forearm
EES
Hand
d
Temperature (°C)
36
35
34
33
32
31
IR camera
EES
0
20
40
60
Location (mm)
e
Channel #1
#3
#5
Forearm
Wet paper towel
f
Thermal conductivity (W/mK)
0.4
0.3
0.2
0.1
Wet paper towel
0
20
40
60
Location (mm)
g
Thermal conductivity (W/mK)
0.4
0.3
0.2
0.1
0.0
50 % ethanol
Acrylic board
Air
0
10
20
Cleaning cycles (trial)
h
Thermal conductivity (W/mK)
0.4
0.3
0.2
0.1
0.0
Forearm
0
10
20
Number of test

Figure 4

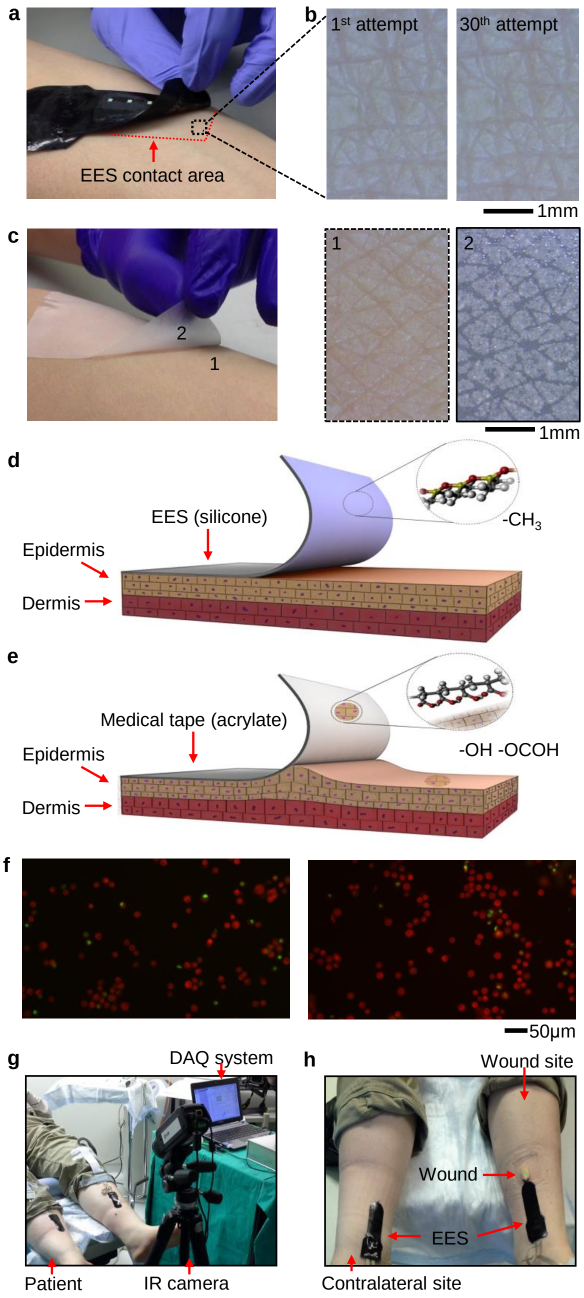

i

Step	Process	Time (min.)
1	Laminate EES device on the skin	1.5
2	Measure higher voltage for TC	3
3	Measure lower voltage for TC	1.5
4	Calculate TC and evaluate	0.5
5	Measure voltage for temperature	0.5
6	Take IR image	1
7	Calculate temperature and evaluate	2
		Total: 10

Figure 5

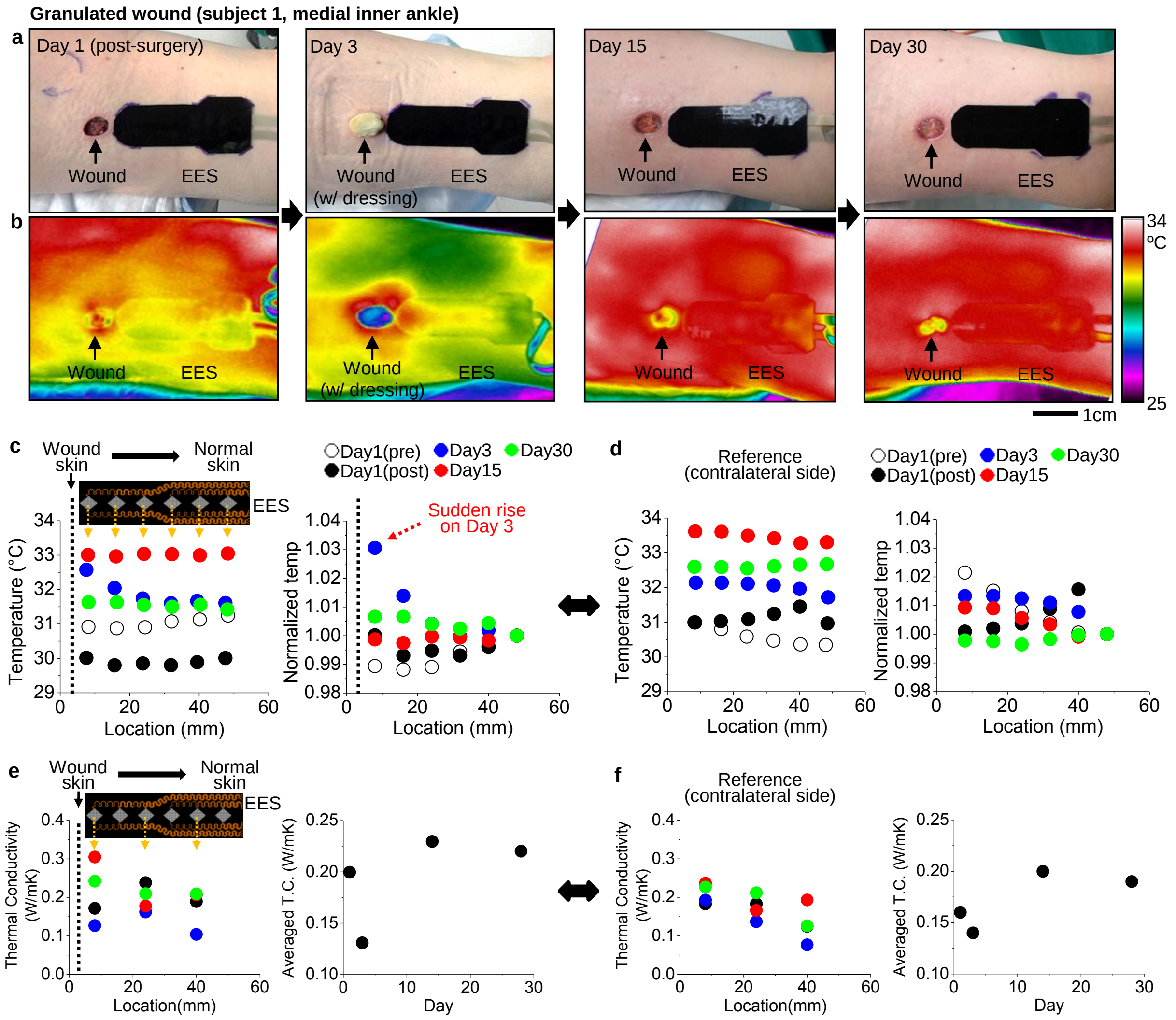
Granulated wound (subject 1, medial inner ankle)
a
Day 1 (post-surgery)
Wound
EES
Day 3
Wound
(w/ dressing)
EES
Day 15
Wound
EES
Day 30
Wound
EES
b
Wound
EES
Wound
(w/ dressing)
EES
Wound
EES
Wound
EES
34
ºC
25
1cm
c
Wound skin
Normal skin
EES
Temperature (°C)
34
33
32
31
30
29
0
20
40
60
Location (mm)
○Day1(pre) ●Day3 ●Day30
●Day1(post) ●Day15
Sudden rise on Day 3
Normalized temp
1.04
1.03
1.02
1.01
1.00
0.99
0.98
0
20
40
60
Location (mm)
d
Reference (contralateral side)
Temperature (°C)
34
33
32
31
30
29
0
20
40
60
Location (mm)
○Day1(pre) ●Day3 ●Day30
●Day1(post) ●Day15
Normalized temp
1.04
1.03
1.02
1.01
1.00
0.99
0.98
0
20
40
60
Location (mm)
e
Wound skin
Normal skin
EES
Thermal Conductivity (W/mK)
0.4
0.3
0.2
0.1
0.0
0
20
40
60
Location(mm)
Averaged T.C. (W/mK)
0.25
0.20
0.15
0.10
0
10
20
30
Day
f
Reference (contralateral side)
Thermal Conductivity (W/mK)
0.4
0.3
0.2
0.1
0.0
0
20
40
60
Location(mm)
Averaged T.C. (W/mK)
0.25
0.20
0.15
0.10
0
10
20
30
Day

Figure 6

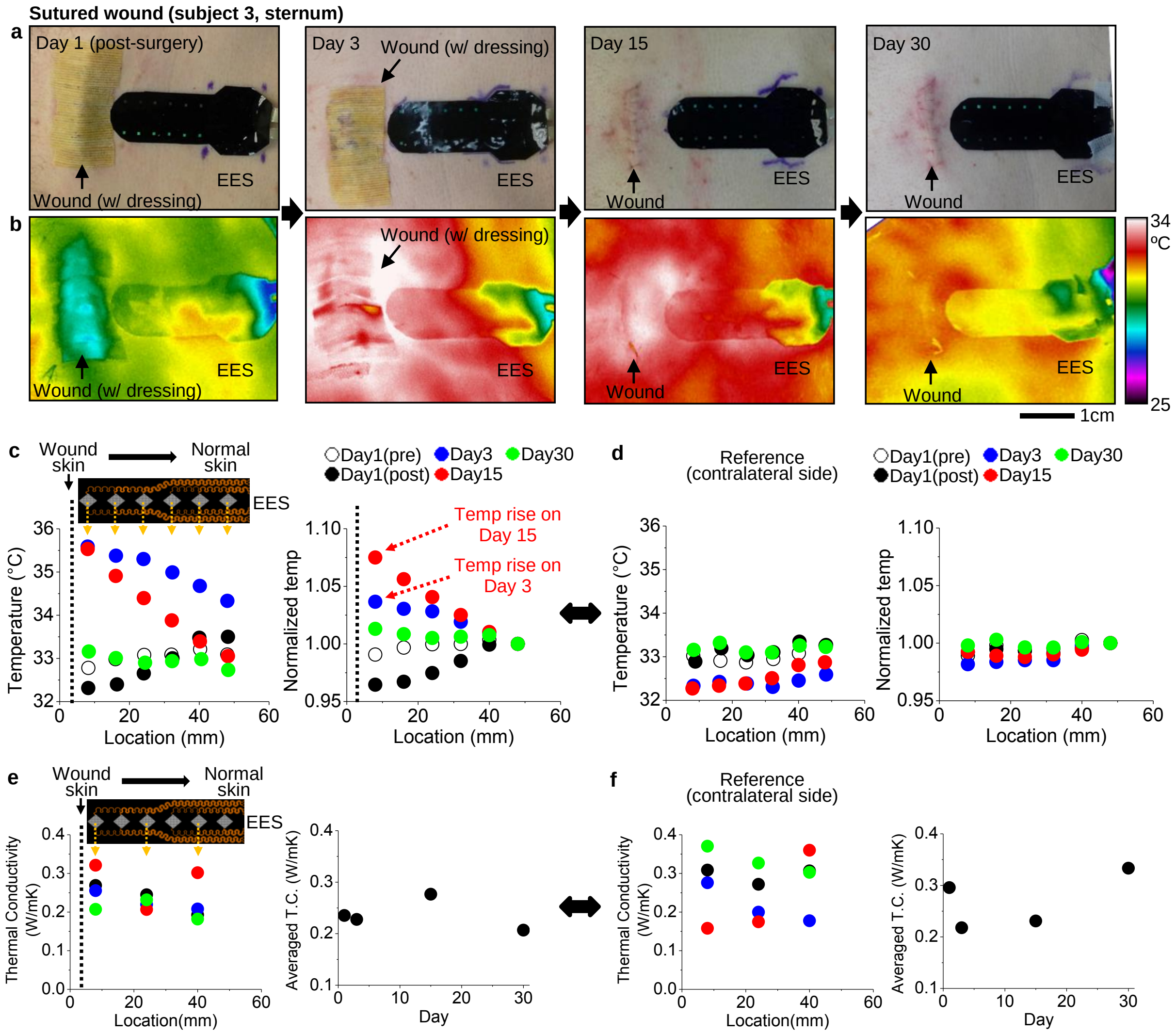
Sutured wound (subject 3, sternum)
a
Day 1 (post-surgery)
Wound (w/ dressing)
EES
Day 3
Wound (w/ dressing)
Day 15
Wound
Day 30
b
34 °C
25
1cm
c
Wound skin
Normal skin
EES
Temperature (°C)
Location (mm)
○Day1(pre) ●Day3 ●Day30
●Day1(post) ●Day15
Normalized temp
Temp rise on Day 15
Temp rise on Day 3
d
Reference (contralateral side)
e
Thermal Conductivity (W/mK)
Location(mm)
Averaged T.C. (W/mK)
Day
f
Reference (contralateral side)

Table 1. Summary of clinical study with 3 subjects.

	Subject 1	Subject 2	Subject 3
Wound type	Granulated	Granulated	Sutured
Age	62	79	54
Sex	Male	Female	Male
Race	White, Caucasian	White, Caucasian	White, Caucasian
Site of lesion	Left medial inner ankle	Right shin	Sternum
Device contact*	Conformal	Conformal	Conformal
Temperature rise	On day 3	On day 15	On day 3 and 15

*Assessment by thermal conductivity measurement

Supporting Information

NOTE 1: FEM analysis of various meandering structures

Mechanical stretchability studied by FEM analysis provides an efficient means for identifying the most appropriate designs in skin mountable device construction. Fig. S1 shows biaxial stretchability in the elastic response regime for four different structures: regular curve, serpentine, fractal (‘all vertical’), and fractal (‘half and half’). The FEM analysis suggests that the fractal case with half and half design motif offers the highest stretchability. We utilized this design in EES for monitoring wound healing.

NOTE 2: Device fabrication procedure

Fabrication process of an EES follows exploits modified versions of otherwise conventional microfabrication techniques, together with processes of transfer printing (Fig. S2 and S3).

a. Prepare a carrier wafer

1. Clean a silicon wafer with acetone, IPA, and DI water.
2. Dehydrate it on a hot plate at 110 °C for 3 min.
3. Prepare polydimethylsiloxane mixture (PDMS; 10:1 ratio of base and curing agent) and de-gas for an hour in a vacuum pump.
4. Spincoat PDMS on the wafer at 3000 rpm for 1 min.
5. Cure it on a hot plate at 150 °C for 30 min.

b. Deposit materials and photolithography

1. Expose UV onto the wafer to make the surface hydrophilic for 3 min.
2. Spincoat polyimide at 4000 rpm for 1 min.
3. Pre-bake it on a hot plate at 150 °C for 5 min.
4. Hard bake it in a hot oven at 250 °C for 2 hours.
5. Deposit 3 µm-thick copper (Cu) using an electron beam evaporator

6. Spincoat photoresist (AZ 4620) at 900/1100/4000 rpm for 10/60/20 seconds.
7. Cure it on a hot plate at 75 °C for 30 min.
8. Align and expose UV (fractal and FS interconnect patterns).
9. Develop it a base developer (AZ 400K).
10. Remove photoresist using acetone.
11. Spincoat 2nd layer of polyimide at 2000 rpm for 1 min.
12. Pre-bake it on a hot plate at 150 °C for 5 min.
13. Hard bake it in a hot oven at 250 °C for 2 hours.
14. Spincoat photoresist (AZ 4620) at 900/1100/4000 rpm for 10/60/20 seconds.
15. Cure it on a hot plate at 75 °C for 30 min.
16. Align and expose UV (encapsulation patterns on the pre-patterns).
17. Develop it a base developer (AZ 400K).
18. Etch the patterned two layers of polyimides using reactive ion etcher (RIE, March) at 150 W, 170 mTorr, 20 sccm oxygen for 1500 seconds.

c. Prepare a target silicone substrate

1. Prepare a petri dish to hold silicone material
2. Mix part B, add part A, and mix together thoroughly (Solaris, Smooth-On). Add a black ink with one to one volume ratio. Spincoat the mixture in petri dish at 300 rpm for 1 min, which offers ~500 µm-thick substrate. Cure it at room temperature.
3. Gently detach silicone from the petri dish.

d. Retrieve and transfer print patterns onto the silicone substrate

1. Attach a water soluble tape (3M) onto the patterns on a PDMS/silicon wafer.
2. Put them on a hot plate at 130 °C for 3 min.
3. Rapidly detach the tape to pick up the patterns.
4. Deposit Ti / SiO2 (5 / 50 nm) using an electron beam evaporator.
5. Expose UV onto the targeted silicone for 3 min.

6. Transfer the patterns on it.
7. Dissolve the tape put them in water for 3 hours.
8. Bond flexible, anisotropic cable (Elform) using a hot iron.

NOTE 3: MicroXCT imaging process

Micro X-ray tomography (MicroXCT 400, Xradia, USA) provides an attractive method for imaging the 3D spatial topology of various fractal structures under different states of deformation. Experimental images in Fig. 1F and 1G demonstrate the structural details of fractal patterns observable using the MicroXCT system. 0.5 X magnification provides views of the entire structures. Additional imaging parameters include a 40 KeV X-ray source and 200 μA current, with 600 image frames recorded stepwise over 180 degrees. The TXM Reconstructor software embedded in the system reconstructs the images, and the visualization software package (Amira 5.4.2, Visage Imaging) yields the “gray-scale” images.

NOTE 4: Calibration set up and procedure for temperature measurements

A peak-to-peak current of 50 μA with 997 Hz, which causes minimal self-heating (*Supplementary Fig. S6*), is applied to the circuit for the temperature measurement. Here, the fractal sensor serves as a resistance thermometer. The resistance is calculated from the measured voltage. Calibrations are performed with a hotplate that enables control to within 1 ºC. The EES device is mounted with the sensor side up on a flat black plate with emissivity of 0.96. The setup enables reduction of resistance changes associated with mechanical deformation in the mounting step, thereby providing improved precision in calibration. The set up does, however, induce some relative error in the temperature measurement because the surface temperature of the device is typically ~0.3 °C lower than the surface of the black plate, due to convection (details in *Supplementary Note 9*). As a result, a temperature calculated by the calibration lines is slightly higher than the actual temperature. The calibrations include 7 temperature points between 30 °C and 48°C. After allowing thermal equilibration for 10 min, the surface temperature on the black plate near the device is recorded by the IR camera. In the meantime, the voltage of each sensor is recorded for 20 seconds. The linear function that determines the temperature is obtained by least squares method. The precision of measurements with an EES is about 50 mK based on limitations in the analogue-to-digital converter. Absolute accuracy, based on the error of current output, is ~200 mK.

NOTE 5: Thermal conductivity measurement and calibration procedure

The thermal conductivity (λ) of the skin is measured using a modified version of the 3 omega method. The 3 omega method has been used extensively for measuring the thermal conductivity of a wide variety of thin films as well as bulk solid materials, liquid (*27, 46*), and gas (*47*). When a sinusoidal current with 1ω is applied to a resistive heating element, the temperature increases by Joule heating at 2ω. The frequency dependence of the amplitude of this 2 temperature oscillation ($\Delta T_{2\omega}$) depends on the thermal property of a material of interest bonded to the heater. Measurement of the temperature oscillation is performed at the 3ω oscillation associated with the voltage drop in the resistive element (metal line). The 3ω voltage oscillation is induced by the original current oscillations of 1ω and the change of the metal line resistance at 2ω. *Supplementary Fig. S7* shows the frequency dependence of the fractal-base sensor on amplitude of voltage at 3ω for the case of exposure to air. The $\Delta T_{2\omega}$ is expressed by the following equation (*46*):

$$\Delta T_{2\omega} = 2\frac{V_{3\omega}}{I_{rms}}\frac{dT}{dR} \qquad \text{(S5-1)}$$

where $V_{3\omega}$ is the measured rms voltage at 3ω, and I_{rms} is the applied rms current at 1ω. dT/dR is the change in temperature as a function of resistance. *Supplementary Fig. S8* shows the temperature amplitudes at 2ω as a function of frequency for air and water. The shape of the curve depends on the properties of the sample under test in addition to the design of heater and the thin insulation layer between sample and heater. The graph of the $\Delta T_{2\omega}$ vs. frequency is often used to estimate the thermal conductivity.

In most cases, the heater is formed directly on the sample of interest by microfabrication (*25*). Here, the temperature oscillation depends on the frequency and the sample, and is related to the thermal conductivity by analytical solution or numerical calculation. When the heater is a simple metal line, the temperature oscillation can be analytically solved by use of a simplified model of the heat transfer equation and a semi-infinite sample. According to the solution, the relationship between $\Delta T_{2\omega}$ and the natural logarithms of the frequency is linear in the low frequency range. The slope gives the thermal conductivity as shown in following the equation.

$$\frac{d\Delta T_{2\omega}}{d\ln f} = -\frac{P_{rms}}{2\pi l\lambda} \qquad \text{(S5-2)}$$

where P_{rms} is the amplitude of the RMS power in the sensor, and l is the length of the sensor. Namely thermal conductivity can be obtained from two 3ω voltages at different frequency as shown in following the equation.

$$\lambda = \frac{R_0 I_{rms}^3 \ln(f_H/f_L)}{4l\pi(V_{3wL}-V_{3wH})}\frac{dR}{dT} \qquad \text{(S5-3)}$$

where R_0 is the nominal resistance of the sensor. The subscript *H* and *L* indicates higher and lower frequency.

It is expected that the fractal-base sensor can be used to estimate thermal conductivity from the $\Delta T_{2\omega}$ depends on frequency. However, it is difficult to obtain the relationship between oscillation temperature and thermal conductivity analytically because the design and structure is more complicated. Therefore, we estimate the thermal conductivity under the assumption that equation S5-3 can apply to the fractal-base sensor in a range of 0.1 Hz to 50 Hz. The relationship between oscillation temperature and the logarithm of frequency in this range is curved, as in the *Supplementary Fig. S8*. In the linear heater, the transition range depends on the width of the heater (*25*). The transition range for the linear heater usually falls between 100-1000 Hz. The transition range for the fractal-base sensor may occur at reduced frequencies because the sample is heated across the entire area of the fractal heater. Meanwhile, a quick measurement is desired in terms of the clinical study. For this purpose, higher frequencies should be selected since the lower frequencies demand longer times to measure the 3ω voltage precisely. For this reason, the transition range is considered in this study. When equation S5-3 is applied to the transition range, the calculated thermal conductivity is influenced by the selected two frequencies. For example, the thermal conductivity is calculated to be 0.48 W/mK for 0.3 Hz and 1 Hz. The value becomes 0.28 W/mK for 0.5 Hz and 1 Hz. The relationship of calculated value and real value is investigated by measurements of air and the mixtures of water and ethanol at multiple combinations of frequency. When a liquid is measured, the device floats on the liquid. The device hangs suspended in air for the air measurement. The 3ω voltage is measured with proper time constant and recording time at room temperature. The mixtures of ethanol and water with weight percentages of 0 %, 25 %, 50 %, 75 % and 100 % ethanol were used in the test. The real values of the mixture are known from previous studies using different measurement techniques (*26*). *Supplementary Fig. S9* shows the relationship between the calculated value and the actual value. The results exhibit excellent correspondence and can be used to estimate the actual thermal conductivity empirically.

NOTE 6: Cylindrical 2D model for fractal-base sensor and numerical analysis of penetration depth for 3 omega method

Here, the penetration depth for the skin thermal conductivity measurement by the 3ω method is discussed. In the 3ω method, the thermal conductivity is estimated based on the oscillation temperature distribution near the heater. A numerical simulation for the 3ω method was conducted to clarify the distribution of the oscillating temperature in the skin and to support the empirical modification of the 3ω method described above. The heat transfer of unsteady condition can be described with the following equation.

$$\nabla(\lambda\nabla \mathrm{T}) + \frac{q}{\lambda} = \rho C \frac{\partial T}{\partial t} \tag{S6-1}$$

where ρ is the density, C is the heat capacity, t is the time, and q is the power density. The convective heat transfer of blood capillary in a skin is neglected. The above conduction equation is modified into a quasi-steady-state form with complex coefficients to directly solve the oscillation temperate (*27, 28*).

$$\nabla\left(\lambda\nabla\tilde{T}\right) - i2\omega\rho C\tilde{T} + \frac{\tilde{q}}{2} = 0 \tag{S6-2}$$

where $\tilde{T}$ is the complex oscillation temperature, $\tilde{q}$ is the amplitude of sinusoidal power density with 2ω. The governing equation is solved under a 2D model for the fractal-base sensor with a cylindrically symmetric (r, z) geometry. In the 3ω method, AC power heats a long and thin heater. The sample under test is heated this element (width w of 35 μm, height h of 3 μm, length l of 103 mm) with power density of q in a square area with side of a (3.5 mm). In the 2D model, the fractal-base heater is treated as multiple concentric rings as shown in *Supplementary Fig. S10*. To simulate the actual heater, the width, height and length of the original fractal shape and the heated area are retained. The interval of the heater rings is described by following equation,

$$\sum_{k=1}^{n}\left(\frac{b}{2} + \frac{w}{2} + (w+b)(k-1)\right)2\pi = l$$

$$\left\{b\left(n - \frac{1}{2}\right) + wn + c\right\}^2 \pi = a^2 \tag{S6-3}$$

where b and c are the interval of heater, and n is the number of concentric rings. The first and second equations describe the heater length and area, respectively. For the present case, b and c and n are calculated to be 79.1 μm, 73.9 μm and 17. Therefore, the fractal shape is expressed by 17 concentric rings. The skin model includes the epidermis, dermis, subcutaneous fat and muscle layer. The governing equation S6-2 is solved by the finite volume method with a line-by-line algorithm. The boundary conditions are adiabatic along the cylindrical axis, the right lateral surface and top surface, and isothermal at the bottom at zero temperature increase. The calculation area is divided by 413×87 variable-size grid. A harmonic average of thermal conductivity was used at the interfaces between different materials. The material properties and the thicknesses of layers used in the simulations are presented in Supplemental Table S1. The physical properties are assumed to be constant throughout the calculation. $\tilde{q}$ is calculated by following equation.

$$\tilde{q} = \frac{I_0^2 R_0}{whl} \tag{S6-4}$$

where I_0 is the amplitude of sinusoidal peak-to-peak current. The simulated oscillation temperature for air and water is displayed in *Supplementary Fig. S8*. The simulated temperature corresponds to the average of all concentric rings. The transition range of 0.5-100 Hz compares favorably with that seen for the fractal-base sensor. The computed oscillation temperature for the skin is displayed in Fig. 2e and *Supplementary Fig. S11 and S12*. The amplitude of the oscillating temperature surrounding the heater decreases sharply in the epidermis and the dermis layer. The characteristic temperature distribution is similar to that described in previous studies on different systems (*28*). This result indicates that frequencies of 1 and 3 Hz, i.e. those used in clinical study, yield a thermal conductivity that includes an average through both the epidermis and the dermis.

NOTE 7: Numerical simulation for expecting the temperature of skin tissue heated by EES

The temperature of skin heated by EES is calculated by following well-known Pennes bioheat transfer equation.

$$\nabla(\lambda \nabla T) + \rho_b C_b \omega_b (T_b - T) + q_{met} + q = 0 \tag{S7-1}$$

where ρ_b is the density of the blood, C_b is the heat capacity of the blood, ω_b is the volumetric blood, T_b is the temperature of artery, q_{met} is the power density of metabolic heat generation, and q is the power density from EES. The governing equation is solved by FVM under the developed 2D model. The model and calculation methods are similar to those used for the analysis of penetration depth, but the boundary conditions are different (Supplementary Fig. S12). The boundary conditions are adiabatic along the cylindrical axis and the right lateral surface, and isothermal at the bottom at a constant body temperature T_c. Convection and radiation are considered at the skin and air interface. The following boundary condition is imposed to the top of EES.

$$-\lambda \frac{\partial T}{\partial z} = h_{con}(T - T_{air}) + h_{rad}(T - T_{air}) \tag{S7-2}$$

where h_{con} and h_{rad} is the heat convection coefficient and the radiative heat transfer coefficient between the skin surface and the surrounding air, respectively. T_{air} is the surrounding air temperature. The first term heat convection coefficient corresponds to the effect of natural and forced convection. The heat convection coefficient and radiative heat transfer coefficient of human skin are treated as constant values, set to 4.0 W/(m^{2}K) and 4.7 W/(m^{2}K), respectively (*48, 49*).

The aim of the simulation is to acquire knowledge concerning the general relationship between the surface temperature of the device and the temperature distribution inside the skin. Since it is difficult to measure all necessary parameters, we attempted to fit the simulation results to the measured surface temperatures by assigning appropriate values. The experimental value, $R_0 = 17.7\ \Omega$, $I_0 = 35$ mA, $T_{air} = 25$ ºC are given. q is calculated by the following equation,

$$q = \frac{I_{\mathrm{rms}}^2 R_0}{whl} \tag{S7-3}$$

Typical biological values, $T_c = T_b = 37$ ºC are used. The other material properties and the length of layer are displayed in Supplemental Table S1. In the calculation, typical biological values are used. Most of the parameters have a small influence on the surface temperature, except for ω_b of dermis. Therefore the calculated surface temperature is matched to the experimental value by only adjusting the value of ω_b of dermis. This approach is rationalized by homeothermism, in which a constant body temperature is maintained by adjusting the blood flow rate of the dermis against ambient environment.

Supplementary Fig. S13 shows the surface temperature distribution on the device for experiment and numerical results. When ω_b of dermis set 1.7 l/(sm^3), the simulated surface temperature matches experimental value well. The value is in an expected range for the dermis (*49, 50*). In addition to 35 mA, experiments and simulations for different powers were conducted. The simulations for 50 mA and 65 mA calculated using the same value of ω_b of dermis agrees with the experimental results. This outcome validates the approximation of fractal shaped heater in terms of concentric rings. The temperature distribution in the skin appears in Fig. 2g and 2h.

NOTE 8: Setup and procedure for mechanical test on temperature shift

Fig. S14 shows the electrical circuit that was used for the mechanical testing. A constant voltage source embedded in the lock-in amplifier was used instead of the current source to measure the resistance. A constant voltage of 4.5 V at 997 Hz is applied to the circuit. The current flows the circuit is controlled by a 157 Ω resistor. The device is mounted on the stretcher. The contribution of cyclic loading of uniaxial tensile strains up to 15 % is tested. The bending effect is investigated as well. The device is mounted on the plastic sheet with a thickness of 0.2 mm with the sensor side down. The plastic sheet is attached on the stretcher. The plastic sheet and device bend by controlling the stretcher. The deformation on bending radius from 15 mm to 30 mm is investigated.

NOTE 9: The effect of thermal convection on temperature calibration and measurement by EES

Supplementary Fig. S16 shows the temperature on the dotted line in Fig. 3C for EES and infrared camera. The blue line is for the original infrared camera temperature. Although temperature readings from the six sensing components of the EES matches well with the shifted infrared data, there exists some discrepancy, typically 0.6±0.4 ºC. The discrepancy arises from contributions of thermal convection and detailed conditions for the IR camera e.g. camera angle, adjustment of focus, distance to the subject. The discrepancy is investigated by the numerical calculation using a simplified 1D model. In the skin temperature measurement or temperature calibration, the surface temperature of the EES is lower than the skin or the surface temperature of the hotplate. The temperature distribution in the EES is calculated by the following unsteady heat transfer equation.

$$\nabla(\lambda\nabla \mathrm{T})+\frac{q}{\lambda}=\rho C\frac{\partial T}{\partial t} \qquad \text{(S9-1)}$$

The governing equation is solved by the finite volume method with the TDMA algorithm. *Supplementary Fig. S17(A) and (B)* show the simulation model for skin measurement and calibration, respectively. The calculation area is divided into a 43 variable-size grid. The following initial condition and boundary conditions are imposed to the top,

$t = 0$, $T = T_{air}$

$z = 0$, $\mathrm{t} > 0$, $T = T_c$

$z = z_{sur}$, $\mathrm{t} > 0$, $-\lambda\frac{\partial T}{\partial z} = h_{con}(T - T_{air}) + h_{rad}(T - T_{air})$ (S9-2)

where Z_{sur} is the thickness of the device, and T_c is the skin or hotplate temperature and set to 35 ºC. The heat convection coefficient and radiative heat transfer coefficient are set to 4.0 W/(m^{2}K) and 4.7 W/(m^{2}K), respectively. *Supplementary Fig. S18* shows the change of temperature at the upper layer (red line) and the top of the device (blue line) with time. After equilibrium, the temperature at the EES surface is lower by 0.3 ºC than the upper layer. The temperature discrepancy affects the temperature calibration not only for temperature measurement. The sum of the discrepancy of 0.3 ºC in the calibration and the discrepancy of 0.3 ºC in the measurement is close to the discrepancy in the skin temperature measurement.

Supplementary Fig. S18(A) also reveals the temperature change with time. The temperature at the upper layer achieves steady state (99 % of increase temperature) in 1.0 s. The temperature on the device achieves steady state in 6.0 s. As a result measurements in the clinical studies involved a waiting period of 10 seconds after lamination EES on the skin.

NOTE 10: Procedure for device cleaning

Cleaning of an EES in this clinical study followed the protocols and regulations at the hospital (Dermatology, Northwestern Memorial Hospital, Chicago, IL, USA).

1. Dilute disinfectant solution with water.
2. Spray the solution on an EES and leave it for 10 minutes.
3. Rinse the sensor with water three times.
4. Dry the sensor completely before use.

References

1. Fan, J.A. et al. Fractal Design Concepts for Stretchable Electronics. *Nature Communications*, DOI: 10.1038/ncomms4266 (2013).
2. Jeong, J.-W. et al. Materials and Optimized Designs for Human-Machine Interfaces Via Epidermal Electronics. *Advanced Materials*, **25**, 6839-6846 (2013).
3. Yeo, W.H. et al. Multifunctional Epidermal Electronics Printed Directly Onto the Skin. *Advanced Materials* **25**, 2773-2778 (2013).
4. Song, Y.M. et al. Digital cameras with designs inspired by the arthropod eye. *Nature* **497**, 95-99 (2013).
5. Oh, D.W., Jain, A., Eaton, J.K., Goodson, K.E. & Lee, J.S. Thermal conductivity measurement and sedimentation detection of aluminum oxide nanofluids by using the 3 omega method. *International Journal of Heat and Fluid Flow* **29**, 1456-1461 (2008).
6. Choi, S.R. & Kim, D. Real-time thermal characterization of 12 nl fluid samples in a microchannel. *Review of Scientific Instruments* **79** (2008).
7. Yusibani, E. et al. Application of the Three-Omega Method to Measurement of Thermal Conductivity and Thermal Diffusivity of Hydrogen Gas. *International Journal of Thermophysics* **30**, 397-415 (2009).
8. Cahill, D.G. Thermal-Conductivity Measurement from 30-K to 750-K - the 3-Omega Method. *Review of Scientific Instruments* **61**, 802-808 (1990).
9. Assael, M.J., Charitidou, E. & Wakeham, W.A. Absolute Measurements of the Thermal-Conductivity of Mixtures of Alcohols with Water. *International Journal of Thermophysics* **10**, 793-803 (1989).
10. Gram, R.Q., She, A., Craxton, R.S. & Harding, D.R. Thermal conductivity of solid deuterium by the 3 omega method. *Journal of Applied Physics* **112** (2012).

11. deDear, R.J., Arens, E., Hui, Z. & Oguro, M. Convective and radiative heat transfer coefficients for individual human body segments. *International Journal of Biometeorology* **40**, 141-156 (1997).
12. Lv, Y.G. & Liu, J. Effect of transient temperature on thermoreceptor response and thermal sensation. *Building and Environment* **42**, 656-664 (2007).
13. Fiala, D., Lomas, K.J. & Stohrer, M. A computer model of human thermoregulation for a wide range of environmental conditions: the passive system. *Journal of Applied Physiology* **87**, 1957-1972 (1999).
14. Technical datasheet (Dupont Co.)
15. Haynes, W.M. CRC Handbook of Chemistry and Physics, Edn. 94th (CRC Press, 2013).
16. Technical datasheet (Smooth-On Co.)
17. Mark, J.E. Polymer Data Handbook. (Oxford University Press, New York; 1999).
18. Norton, M.J.T., Kadolph, S.J., Johnson, R.F. & Jordan, K.A. Design, Construction, and Use of Minnesota Woman, a Thermally Instrumented Mannequin. *Textile Research Journal* **55**, 5-12 (1985).

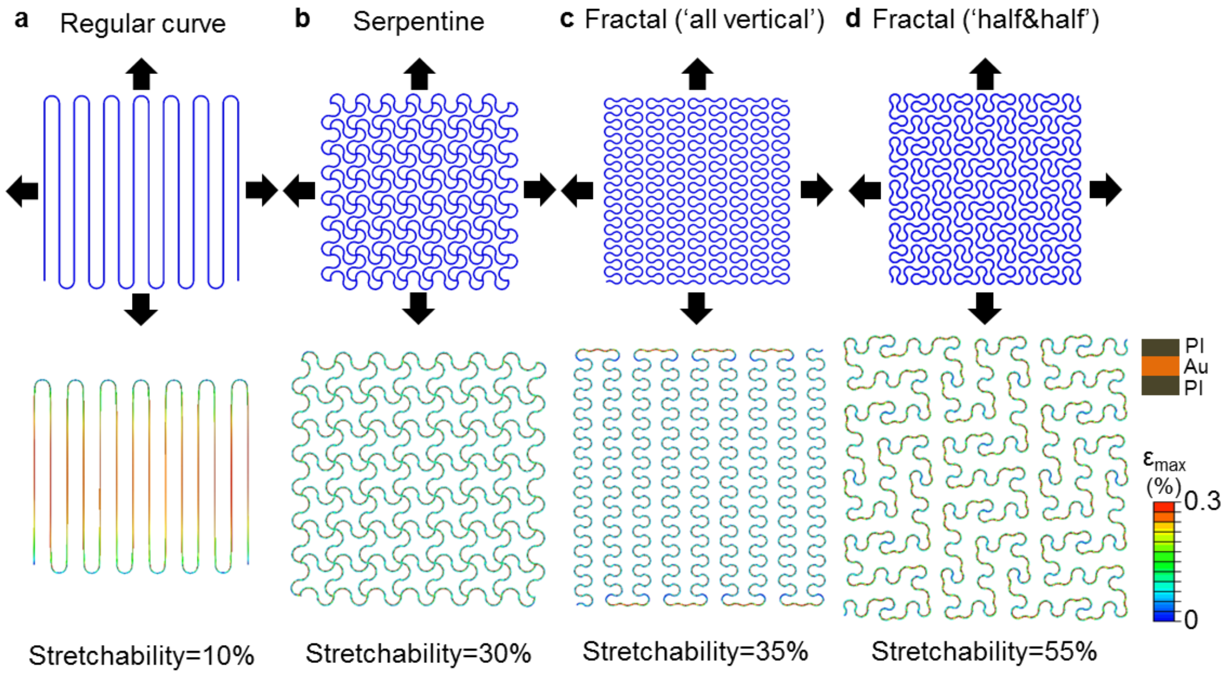

Figure S1. FEM analysis of elastic, biaxial stretching. (a) Regular meandering curve. (b) Serpentine trace. (c) Fractal geometry (Peano curve, 'all vertical'). (d) Fractal geometry (Peano curve, 'half and half').

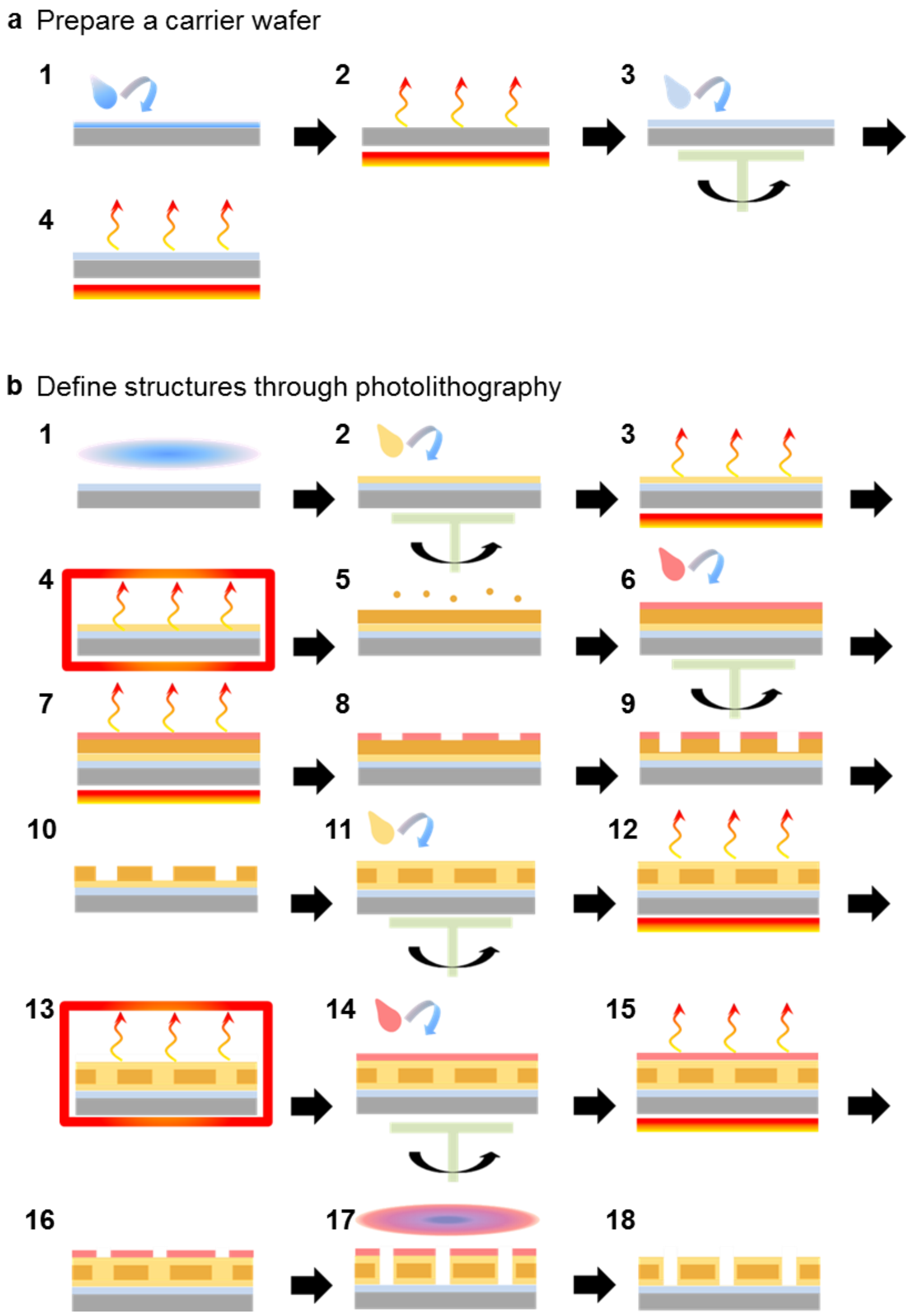

Figure S2. Fabrication procedure (part 1). (a) 1. Cleaning, 2. Dehydration, 3. PDMS spincoating, and 4. Curing. (b) 1. UV exposure, 2. PI spincoating, 3. Pre-bake, 4. Hard-bake, 5. E-beam deposition of copper, 6. PR spincoating, 7. Curing, 8. UV exposure, 9. Developing, 10. PR removal, 11. 2nd PI spincoating, 12. Pre-bake, 13. Hard-bake, 14. PR spincoating, 15. Curing, 16. UV exposure, 17. Developing, and 18. RIE etching of PI.

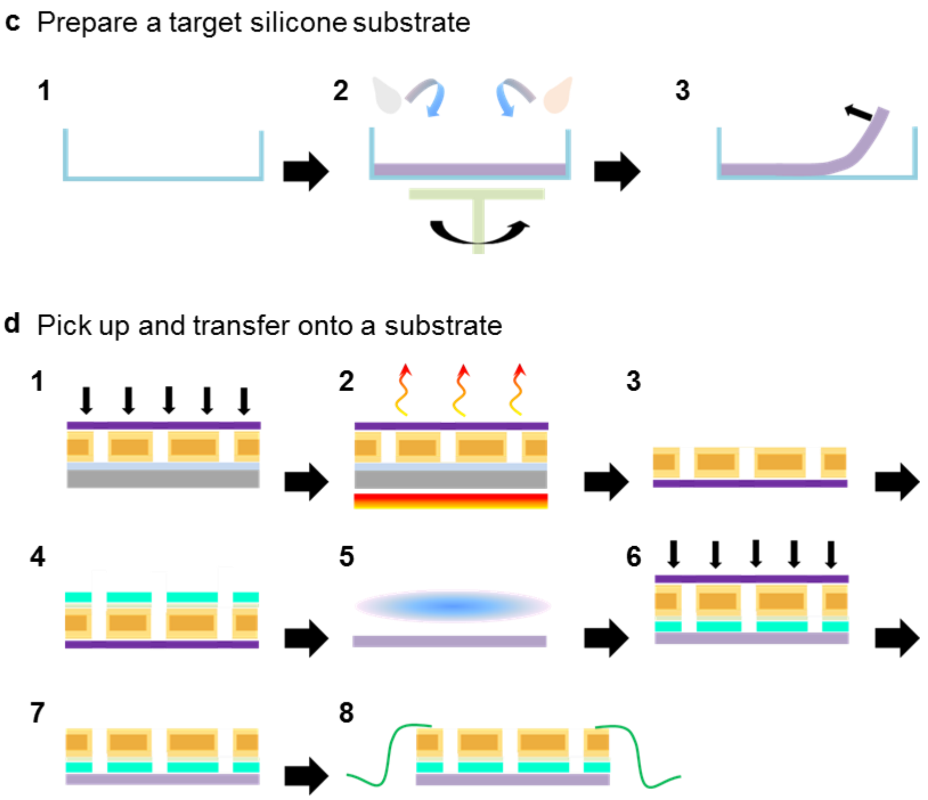

Figure S3. Fabrication procedure (part 2). (c)1. Petri dish preparation, 2. Silicone mixing and spincoating, and 3. Gentle detachment after complete curing. (d) 1. Attachment of water-soluble tape, 2. Heating, 3. Quick detachment of the tape (pattern pickup), 4. E-beam deposition of Ti/SiO_2, 5. UV exposure, 6. Pattern transfer, 7. Tape dissolving in water, and 8. Bonding of a flexible electrical cable.

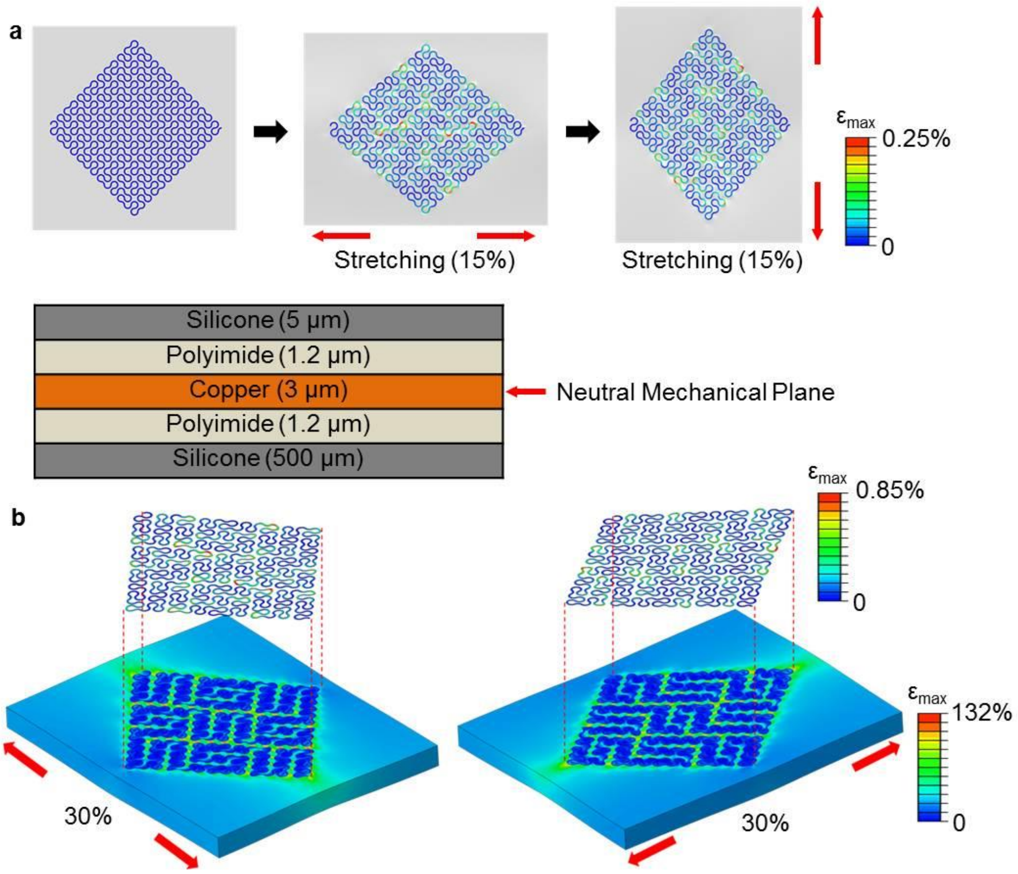

Figure S4. FEM analysis of an EES for wound management. (a) Uniaxial, elastic stretching of fractal patterns in x- and y-directions. (b) Uniaxial stretching of fractals on a silicone membrane.

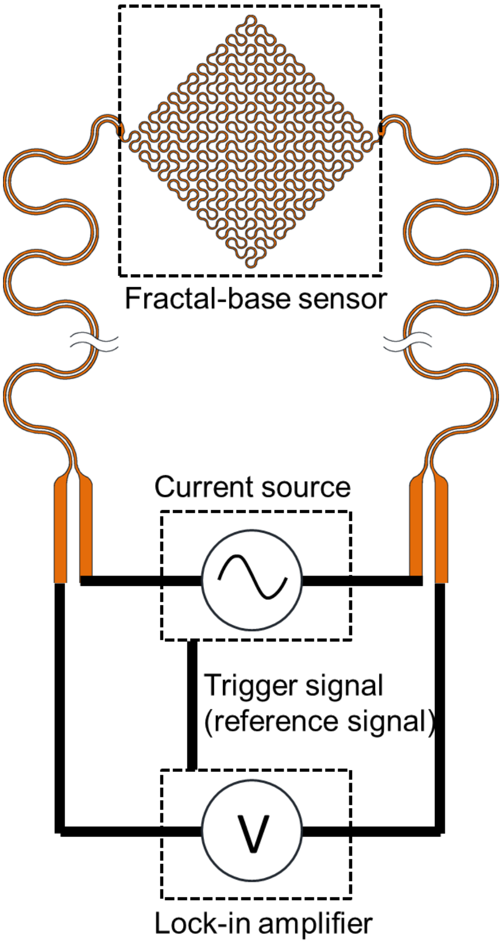

Figure S5. Circuit configuration for voltage measurement across a fractal-based sensor. The voltage drop in the fractal sensor is measured using 4 point-probe technique. The trigger signal generated from the current source is used as a reference signal in the lock-in amplifier.

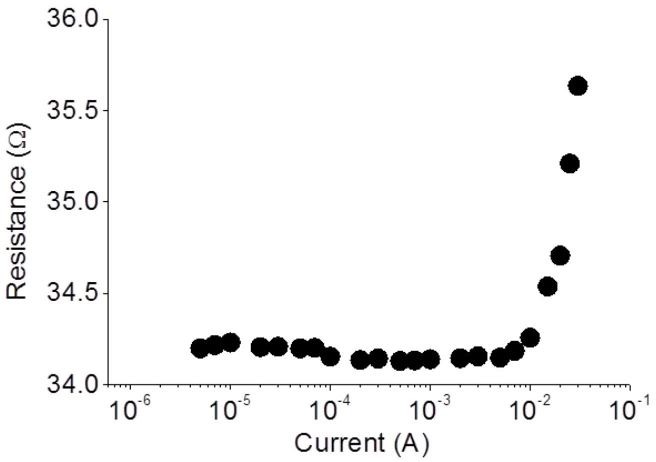

Figure S6. Resistance of fractal-base sensor as a function of current.

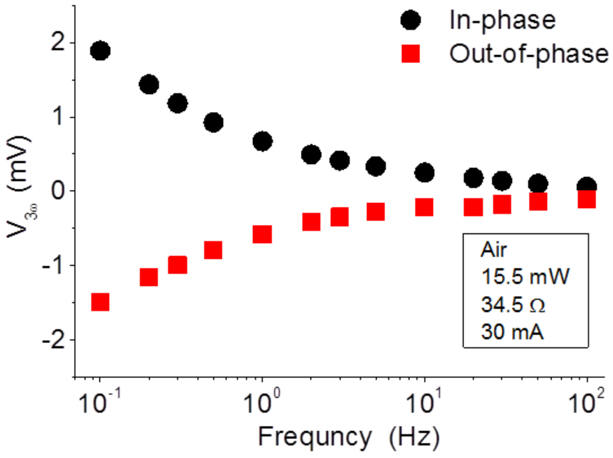

Figure S7. The in-phase and out-of-phase 3 voltage amplitudes as a function of frequency for air.

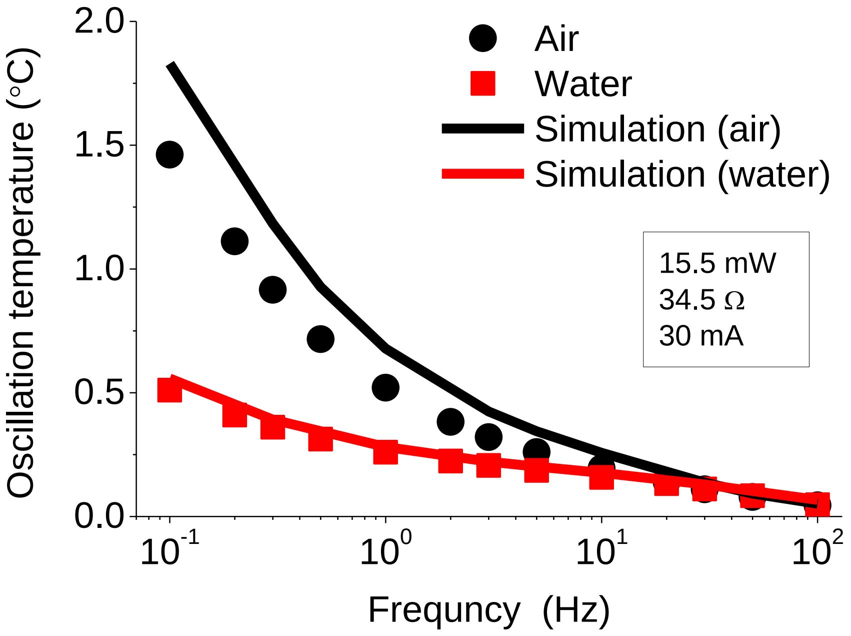

Figure S8. Amplitudes of temperature oscillations at 2ω as a function of frequency for air and water.

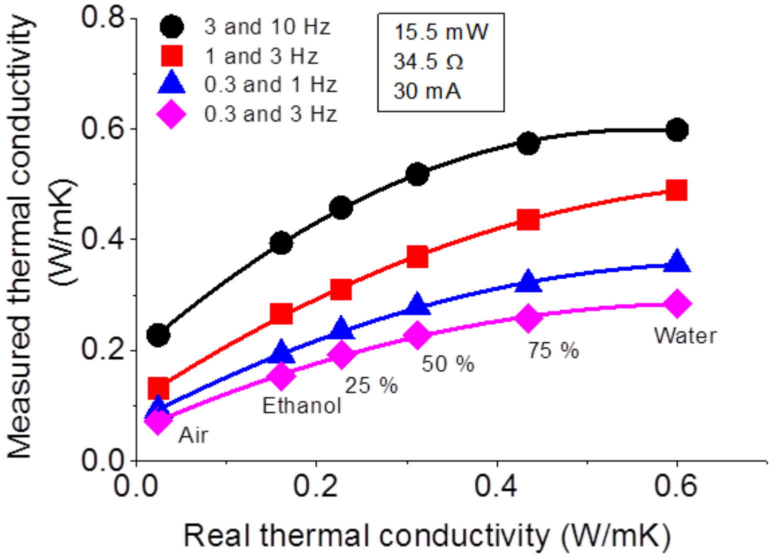

Figure S9. Measured thermal conductivity as a function of the actual (real) value. The thermal conductivity of air and mixtures of ethanol and water with weight percentage of 0%, 25%, 50%, 75% and 100% ethanol were measured by the 3ω method with at various frequencies.

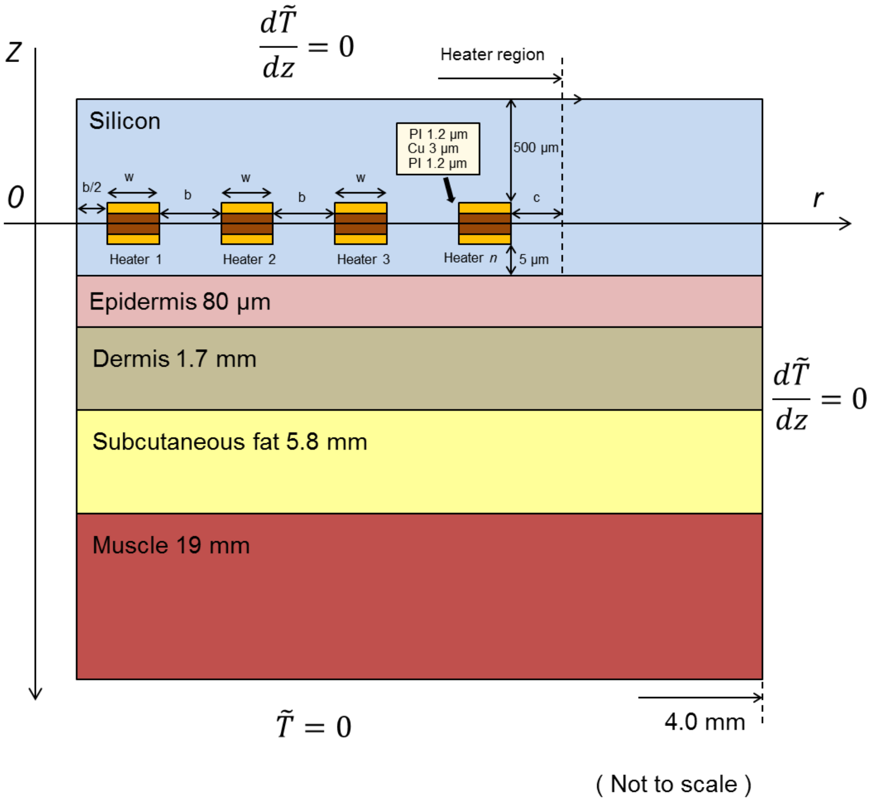

Figure S10. 2D simulation model to approximate the fractal-based sensor for penetration depth analysis.

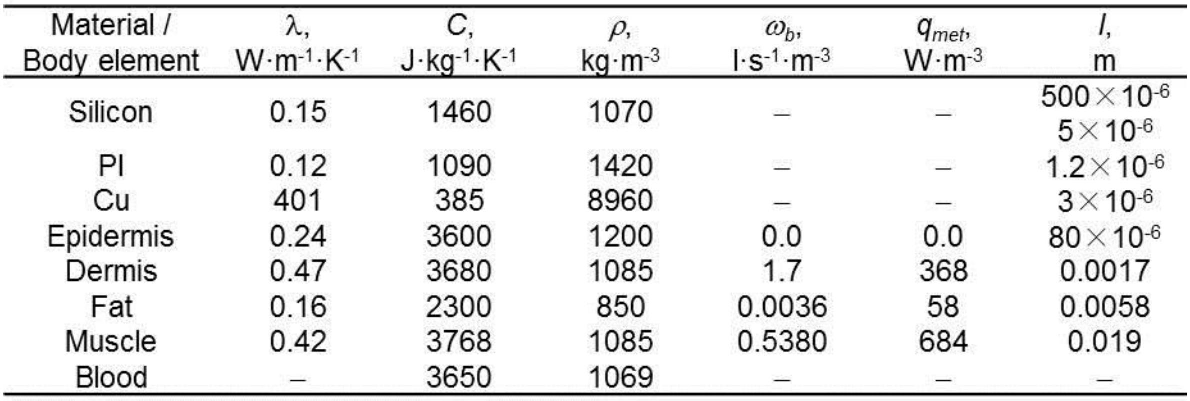

Material / Body element	λ, $W \cdot m^{-1} \cdot K^{-1}$	C, $J \cdot kg^{-1} \cdot K^{-1}$	ρ, $kg \cdot m^{-3}$	ω_b, $l \cdot s^{-1} \cdot m^{-3}$	q_{met}, $W \cdot m^{-3}$	l, m
Silicon	0.15	1460	1070	–	–	500×10^{-6} 5×10^{-6}
PI	0.12	1090	1420	–	–	1.2×10^{-6}
Cu	401	385	8960	–	–	3×10^{-6}
Epidermis	0.24	3600	1200	0.0	0.0	80×10^{-6}
Dermis	0.47	3680	1085	1.7	368	0.0017
Fat	0.16	2300	850	0.0036	58	0.0058
Muscle	0.42	3768	1085	0.5380	684	0.019
Blood	–	3650	1069	–	–	–

Table S1. The geometric and thermal-physical properties of various tissues for the wrist, where is the thermal conductivity, *C* is the heat capacity, is the density, $_b$ is the volumetric blood, q_{met} is the power density of metabolic heat generation, and *l* is the thickness[12-18].

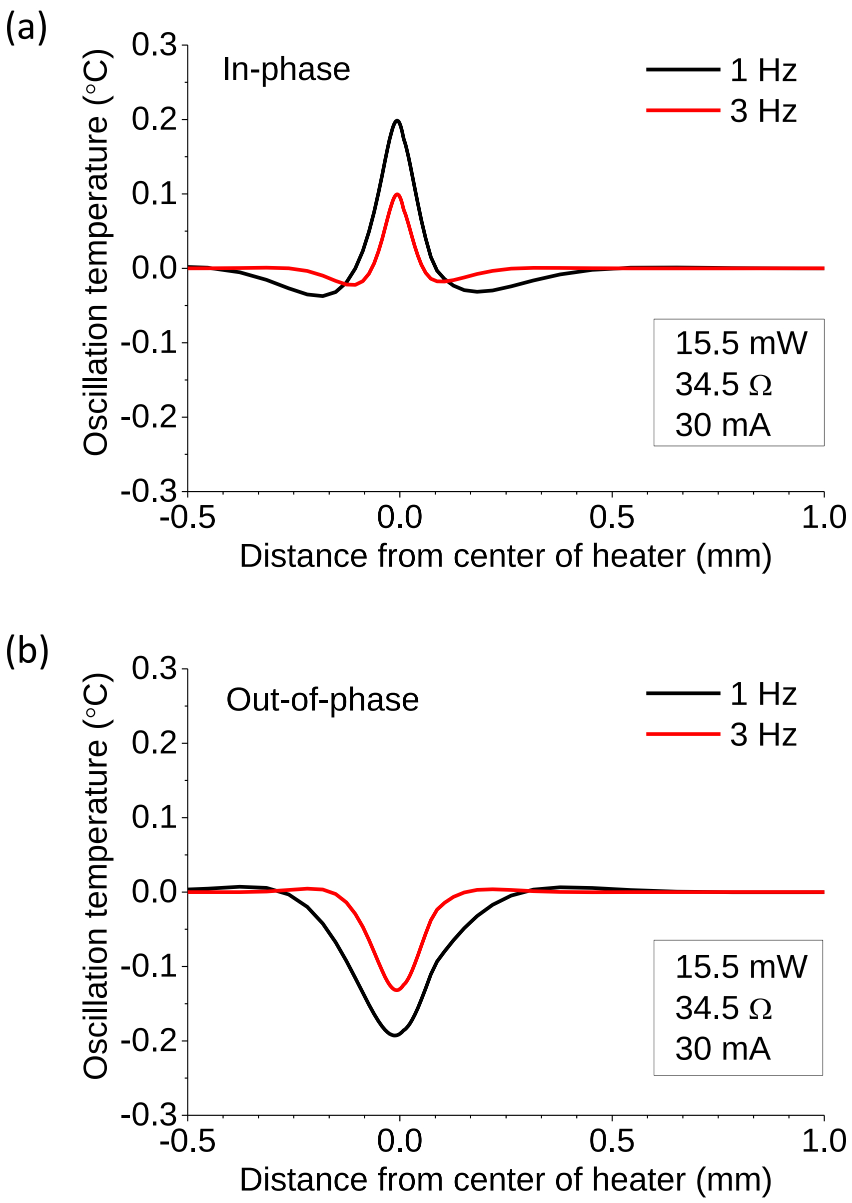

Figure S11. Simulation results for the amplitudes of oscillating temperatures for in phase (a) and out of phase (b) components, as a function of position.

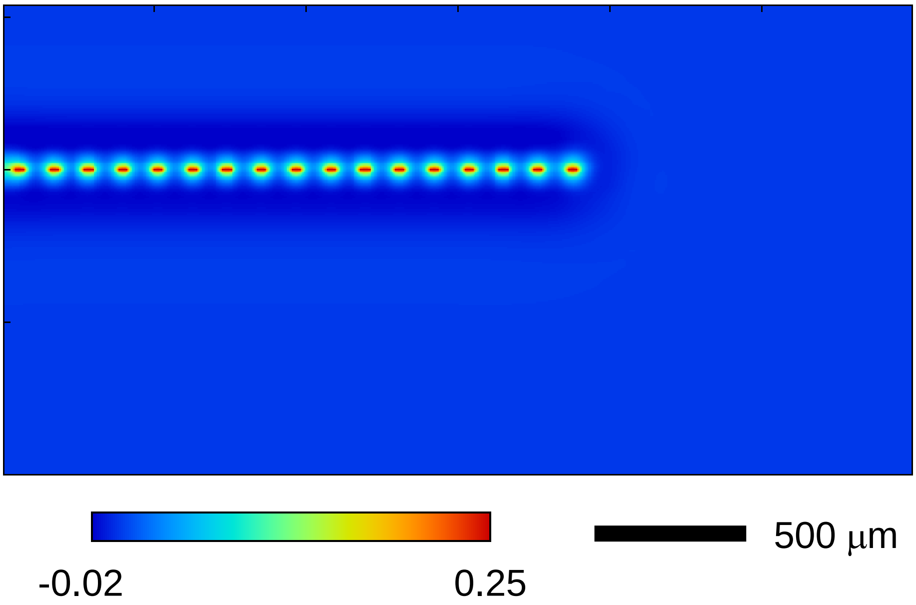

Figure S12. Simulation of the in-phase component of the oscillating temperature distribution near heater for 3 Hz

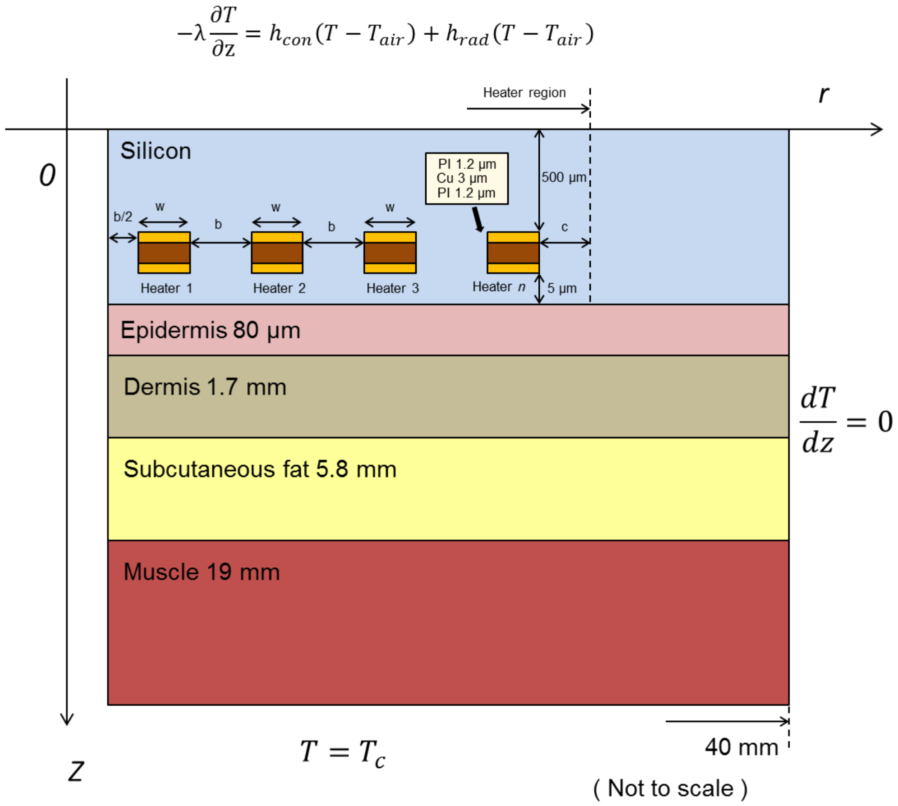

Figure S13. 2D Simulation model to approximate the fractal-based sensor.

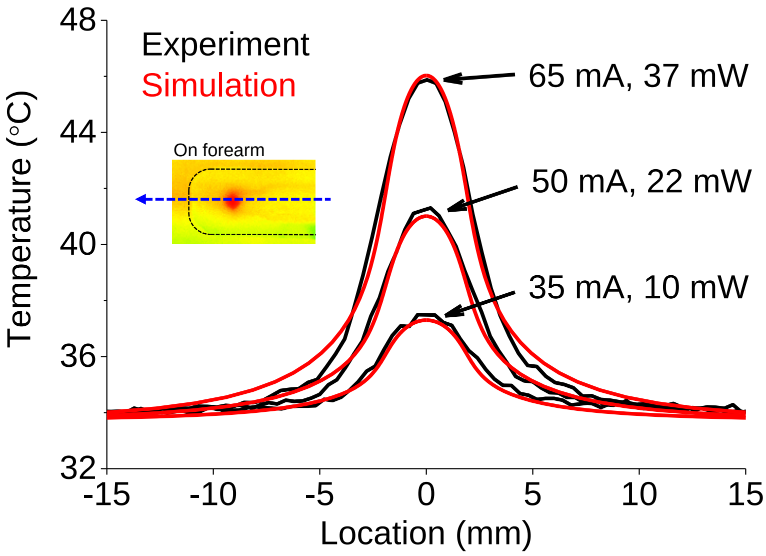

Figure S14. Comparison of experiment and simulation for temperature of an EES on the skin. The horizontal axis shows the distance from the center of the heater on the blue dotted line indicated in insert.

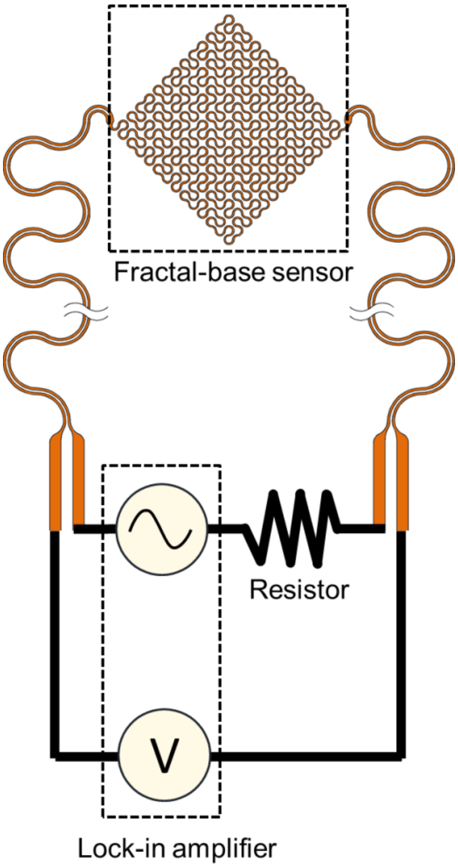

Figure S15. Circuit diagram for mechanical tests.

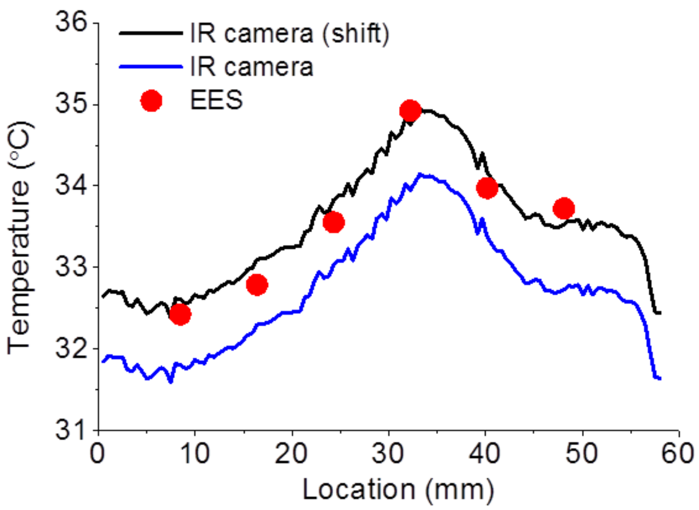

Figure S16. Comparison of temperatures recorded with an EES and an IR camera. The temperature shift arises from stabilization delay and experimental variations with the camera.

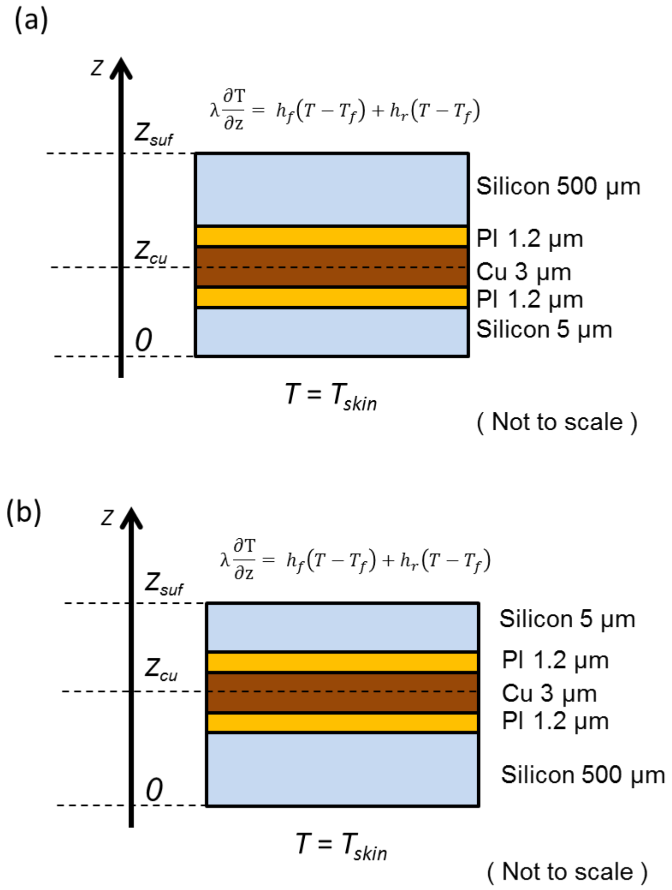

Figure S17. Simulation model for (a) skin temperature measurement and for (b) temperature calibration.

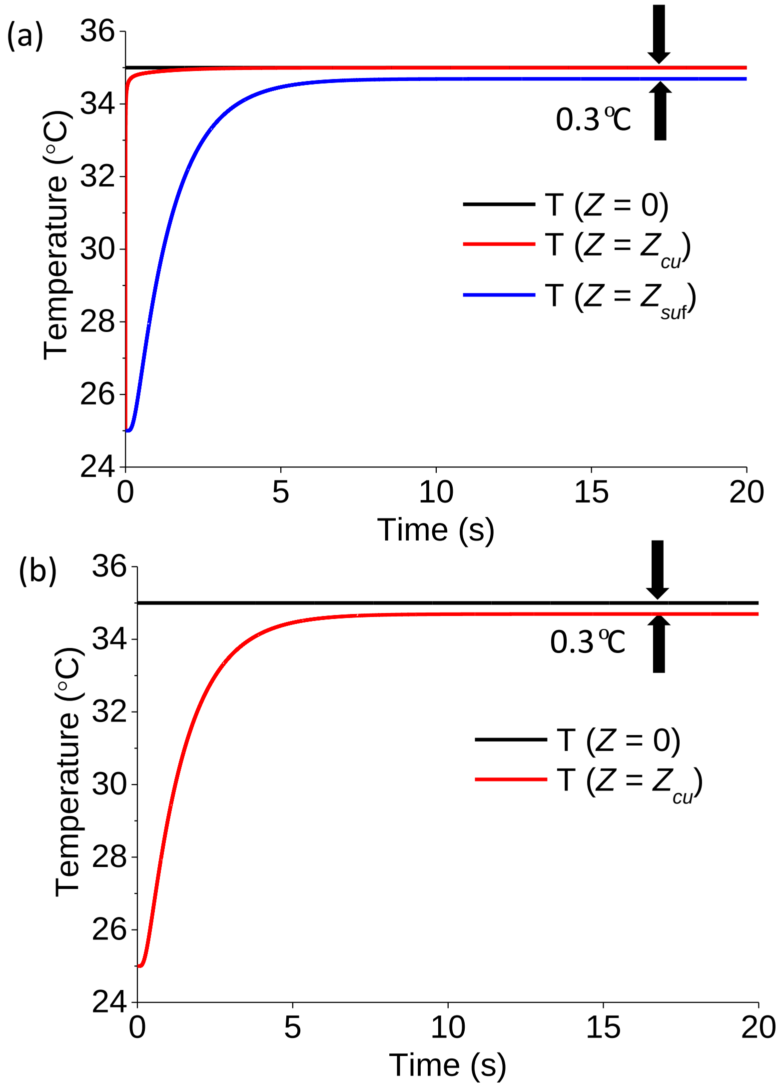

Figure S18. Temperature change with time (a) after laminating the device on skin and (b) mounting the device on the hotplate.

Figure S19. Photo of an EES after spraying with a disinfectant solution (pH Neutral Disinfectant Cleaner, Australian Gold, Indianapolis, IN, USA) for device cleaning.

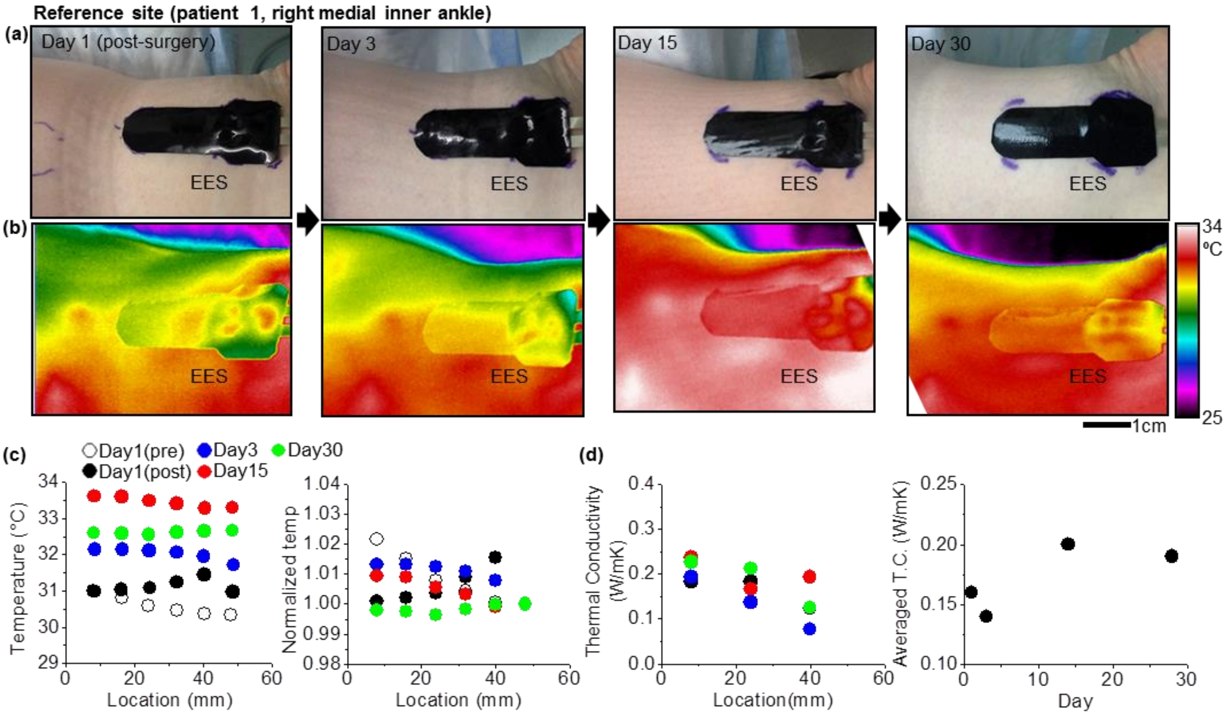

Figure S20. Contralateral (reference site) of subject 1. (a) Representative photographs of a wound with an EES from day 1 to day 30. (b) Corresponding infrared thermographic images of (a) that show the temperature distributions. (c) Temperature distribution recorded with an EES over the course of one month. The device includes six sensors distributed across a length of 45 mm. (d) Thermal conductivity (T.C.) distribution recorded with three sensors in an EES.

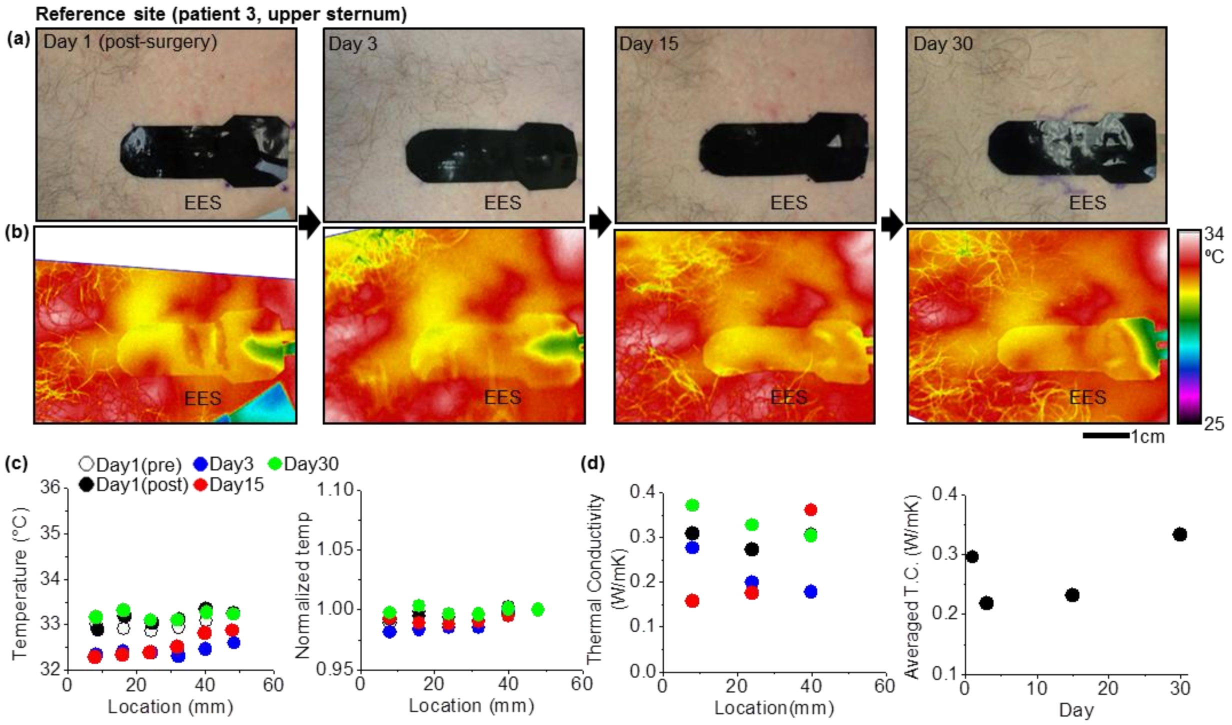

Figure S21. Contralateral (reference site) of subject 3. (a) Representative photographs of wound with an EES from day 1 to day 30. (b) Corresponding infrared thermographic images of (a) that shows temperature distribution. (c) Temperature distribution recorded with an EES over the course of one month. The device includes six sensors distributed across a length of 45 mm. (d) Thermal conductivity (T.C.) distribution recorded with three sensors in an EES.

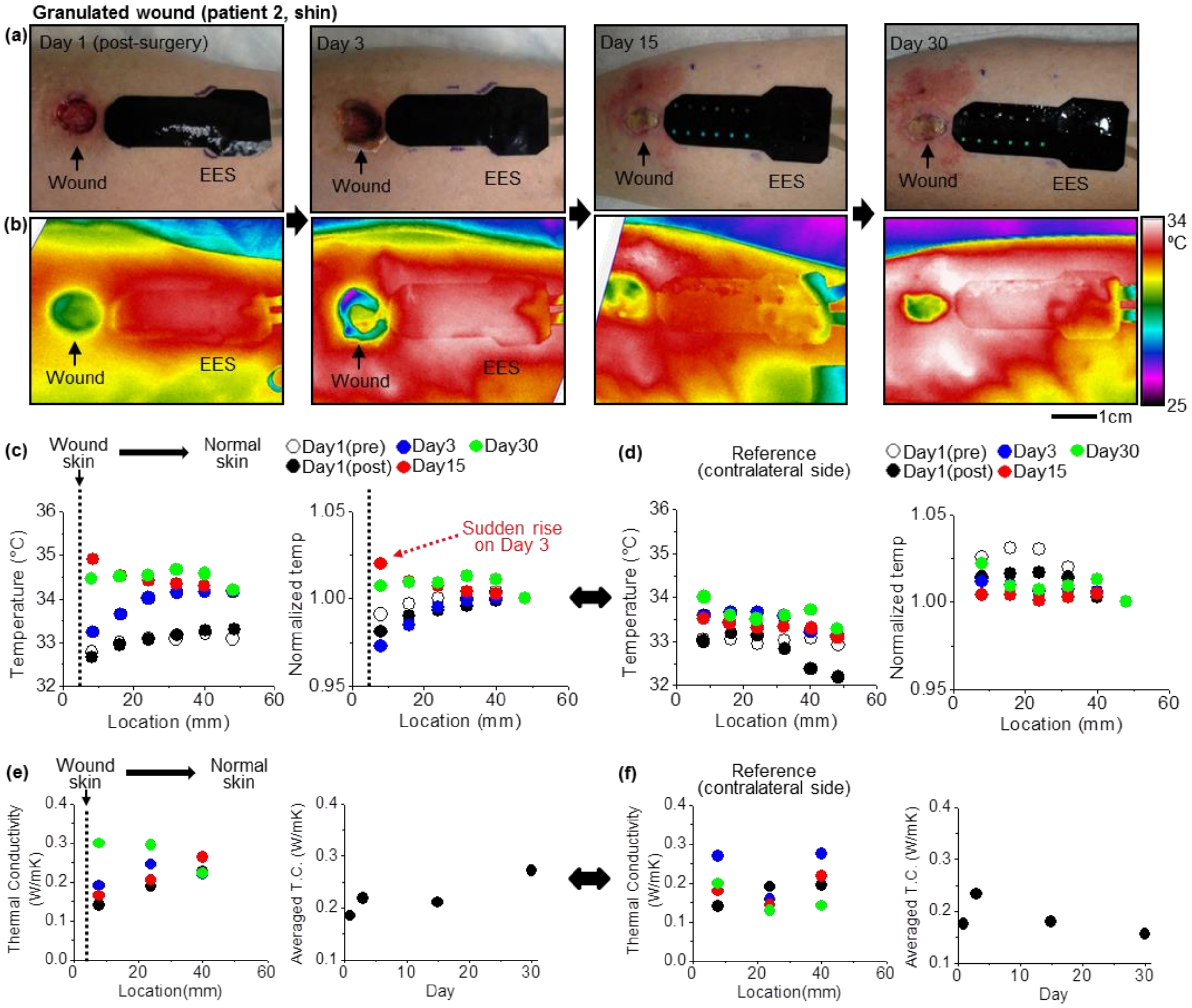

Figure S22. Quantitative management of granulated wound (subject 2) with an EES. (a) Representative photographs of wound with an EES from day 1 to day 30. (b) Corresponding infrared thermographic images of (a) that shows temperature distribution. (c) Temperature distribution recorded with an EES over the course of one month. The device includes six sensors distributed across a length of 45 mm. (d) Temperature distribution on a contralateral side as a control. (e) Thermal conductivity (T.C.) distribution recorded with three sensors in an EES. (f) Thermal conductivity (T.C.) on a contralateral side as a control.